Characterization and source apportionment of aerosol light scattering in a typical polluted city in Yangtze River Delta, China

Dong Chen[1,2], Yu Zhao[1,3*], Jie Zhang[2,3], Huan Yu[4], Xingna Yu[4]

1. State Key Laboratory of Pollution Control & Resource Reuse and School of the Environment, Nanjing University, 163 Xianlin Ave., Nanjing, Jiangsu 210023, China

2. Jiangsu Provincial Academy of Environmental Science, 176 North Jiangdong Rd., Nanjing, Jiangsu 210036, China

3. Collaborative Innovation Center of Atmospheric Environment and Equipment Technology, CICAEET, Nanjing, Jiangsu 210044, China

4. School of Environmental Science and Engineering, Nanjing University of Information Science and Technology, Nanjing, Jiangsu 210044, China

*Corresponding author: Yu Zhao

Phone: 86-25-89680650; email: yuzhao@nju.edu.cn

ABSTRACT

Through online observation and offline chemistry analysis of samples at suburban, urban and industrial sites (NJU, PAES and NUIST respectively) in Nanjing, a typical polluted city in Yangtze River Delta, we optimized the aerosol light scattering estimation method, identified its influencing factors, and quantified the contributions of emission sources to aerosol scattering. The daily average concentration of $PM_{2.5}$ during the sampling period (November 2015-March 2017) was 163.1 ± 13.6 μg/m^3 for the heavily polluted period, 3.8 and 1.6 times those for the clean (47.9 ± 15.8 μg/m^3) and lightly polluted (102.1 ± 16.4 μg/m^3) periods, respectively. The largest increase in PM concentration and its major chemical components was found at the size range of 0.56-1.0 μm for the heavily polluted period, and the contributions of nitrate and sulfate were the greatest in the 0.56-1.0 μm fraction (19.4-39.7% and 18.1-34.7% respectively) for all the three periods. The results indicated that the large growth of nitrate and sulfate were one of the major reasons for the polluted periods. Based on measurements at the three sites, the US Interagency Monitoring of Protected Visual Environments (IMPROVE) algorithm was optimized to evaluate aerosol scattering in eastern China. The light-absorption capacity organic carbon (OC) was estimated to account for over half of the methanol soluble organic carbon (MSOC) at NJU and PAES, whereas the fraction was lower at NUIST. Based on Mie theory, we found that the high relative humidity (RH) could largely enhance the light scattering effect of accumulation particles, but it had few effects on the mixing state of particles. The scattering coefficients of particles within the 0.56-1.0 μm range contributed the most to the total scattering (28-69%). The mass scattering efficiency (MSE) of sulfate and nitrate increased with the elevated pollution level, whereas a low MSE of organic matter (OM) was found for the heavily polluted period, probably because a proportion of OM had only light-absorption property. A coupled model of positive matrix factorization (PMF) and Mie theory was developed and applied for the source apportionment of aerosol light scattering. Coal burning, industry and vehicles were identified as the major sources of the reduced visibility in Nanjing, with an estimated

45   collective contribution at 64-70%. The comparison between the clean and polluted

46   period suggested that the increased primary particle emissions from vehicles and

47   industry were the major causes of the visibility degradation in urban and industrial

48   regions, respectively. In addition, secondary aerosols were a great contributor to the

49   reduced visibility.

50   **1 INTRODUCTION**

51   Atmospheric aerosols play a great role in visibility degradation, radiative balance

52   variation and climate (Liu et al., 2017; Malm and Hand, 2007; Zhang et al., 2017),

53   resulting largely from their light extinction (Seinfeld and Pandis, 2006).

54   Understanding the contributions of individual chemical species to aerosol light

55   extinction is important for policy making to alleviate the reduced visibility in cities

56   with aerosol pollution. Studies have estimated that the aerosol single scattering albedo

57   (the fraction of light scattering coefficient to the total extinction) ranges from

58   0.81-0.93 in urban China (Andreae et al., 2008; Cao et al., 2012; Xu et al., 2002; Xu

59   et al., 2012), implying that the deteriorated visibility primarily results from the

60   scattering effect of aerosols.

61   Aerosol light scattering is greatly affected by its chemical composition and

62   hygroscopic growth (Liu et al., 2008; Tao et al., 2014a). Based on estimation of the

63   mass scattering efficiency (MSE) of different chemical components, previous studies

64   found that nitrate, sulfate, sea salt and organic matter (OM) are the dominant

65   contributors to aerosol scattering. Developed based on the long-term observations in

66   national parks, the US "IMPROVE" (Interagency Monitoring of Protected Visual

67   Environments) algorithm has been applied to calculate the light extinction of chemical

68   species in aerosols (Watson et al., 2002). Two versions of IMPROVE algorithms

69   (IMPROVE1999 and IMPROVE2007 hereinafter) were deduced successively

70   (Lowenthal and Naresh, 2003; Pitchford et al., 2007), and both assumed that OM has

71   no light-absorption capacity and only light-scattering capacity. As part of OM,

72   however, brown carbon (BrC) has been highlighted in recent studies for its light

73   absorption in the near UV region (Alexander et al., 2008; Bond et al., 2006;

3

74   Ramanathan et al., 2007; Zhang et al., 2017), and consideration of the light-absorption

75   effect of OM in the optimization process of the IMPROVE formula could improve the

76   understanding of aerosol optical capacity by chemical species (Yan et al., 2014). In

77   addition, hygroscopic growth is a key factor influencing aerosol light scattering

78   (Schwartz, 1996). Previous studies have shown that the light scattering of sulfate and

79   nitrate in $PM_{2.5}$ could be largely enhanced at high relative humidity (RH) conditions

80   (Titos et al., 2016). Aerosol hygroscopicity is expected to depend largely on the

81   particle size and the abundance of water-soluble chemical components (Swietlicki et

82   al., 2008; Tang, 1996). Through the theoretical calculation, Liu et al. (2014) found

83   that smaller particles were in highly hygroscopic mode, whereas larger particles were

84   in nearly hydrophobic mode.

85   Recently, many studies have been conducted on the relationships between

86   visibility and aerosol light scattering in China (Cheng et al., 2015; Tao et al., 2014b;

87   2014c; Xue et al., 2010; Zhang et al., 2015). They found the abundance of

88   hygroscopic ammonium nitrate (NH_4NO_3) and ammonium sulfate ((NH_4)$_2SO_4$) in

89    $PM_{2.5}$ and their characteristics were the important reason visibility reduction.

90   However, few studies have analyzed the size distribution of aerosol light scattering or

91   quantified the contributions of different emission source categories to the aerosol light

92   scattering, particularly at the varied air pollution levels. The roles of particles of

93   different sizes and origins on visibility degradation remained unclear. To fill this

94   knowledge gap, this study conducted campaigns at three multiple-functional sites in

95   Nanjing, a mega city located in eastern China. Nanjing suffered relatively heavy

96   aerosol pollution in the Yangtze River Delta (YRD) attrited to the massive emissions

97   of anthropogenic air pollutants (Zhao et al., 2015). The mixed sources of primary

98   aerosols (e.g., coal burning) and secondary aerosol precursors (e.g., vehicle and

99   petrochemical industry) make Nanjing a typical city to study the multiple influential

100   factors of aerosol light scattering (Chen et al., 2019). Combining online and offline

101   techniques at different functional regions, the IMPROVE algorithm was optimized

102   taking the light-absorption OM into account. The influences of aerosol size

103   distributions and pollution levels on the aerosol scattering effect were quantitatively

evaluated based on comprehensive analysis of the chemical compositions of particles by size and location. To explore the reasons for the visibility reduction in different functional regions, a new coupled PMF-Mie model was developed and the source apportionments of aerosol light scattering were determined for the clean and polluted periods.

2 METHODOLOGY

2.1 Site description

The campaigns were conducted at three sites in Nanjing, i.e., NJU, PAES and NUIST, representative for the suburban, urban and industrial region, respectively (see the site locations in Figure S1 in the Supplement). NJU (32.07°N, 118.57°E) was on the roof (25 m above the ground) of the School of the Environment building in the Nanjing University campus in eastern suburban Nanjing (Chen et al., 2017; 2019). PAES (32.03°N, 118.44°E) was on the roof (30 m above the ground) of the Jiangsu Provincial Academy of Environmental Science building in western urban Nanjing. The site was surrounded by heavy traffic and commercial and residential buildings (Li et al., 2015). NUIST (32.21°N, 118.72°E) was on the roof of the School of the Environment building in the Nanjing University of Information Science & Technology campus. It was an industrial pollution site influenced by the nearby power, iron & steel, and petrochemical industry plants (Wang et al., 2016a).

2.2 Aerosol sampling and chemical analysis

Pre-combusted (at 500 °C for ~5 h) quartz filters (90 mm in diameter, Whatman International Ltd., UK) were applied for $PM_{2.5}$ sampling. The filter samples were weighed before and after sampling under the constant temperature (23±2°C) and RH (40±3%) for 24 hours conditioning. All the $PM_{2.5}$ samples were collected using the TH-150C sampler (Wuhan Tianhong Ltd., China) at a flow rate of 100 L/min. From November 2015 to March 2017, 282 daily $PM_{2.5}$ samples at the three sites (174 for NJU, 45 for PAES and 63 for NUIST) were collected.

Three sets of ten-stage Micro-Orifice Uniform Deposit Impactors (MOUDI,

Model 110, MSP Corp., USA) were adopted to collect size-segregated particles. The 50% cutoff points of the MOUDI-110 were 18, 10, 5.6, 3.2, 1.8, 1.0, 0.56, 0.32, 0.18 and 0.056 μm. Loaded with Teflon and quartz filters (47 mm in diameter, Whatman International Ltd., UK), MOUDI was operated at a flow rate of 30 L/min. To obtain sufficient particles at each stage for the chemical analysis, every sampling lasted continuously for 24 h from 9:00am. All the MOUDI samplers were cleaned using an ultrasonic bath for 30 min before each sampling. The flow rate was calibrated before each sampling and was monitored with the flow meter during the whole sampling process. Those quality control measures assured that the MOUDI samplers were not blocked during the sampling period and the particles collected in the filter were evenly distributed, even for the heavily polluted period with the $PM_{1.8}$ concentration measured over 120 μg/m^3 (see the samples in Figure S2 in the supplement). Attributed to weather condition and aerosol sampler maintenance, the sampling periods for the three sites were different. Seventy-five sets of particle samples were obtained from December 2015 to February 2017 at NJU, 25 sets were obtained from August 2016 to January 2017 at PAES, and 31 sets were obtained from July 2016 to February 2017 at NUIST. Simultaneous samplings were conducted at the three sites from one week to ten days in each season from summer 2016 to winter 2016-2017. For the remaining time, two MOUDI samplers were applied to collect Teflon and quartz filter samples simultaneously at one of the three sites. Besides, blank filters were applied to correct the possible bias in the analysis of aerosol chemical species. Totally 19 sets of size-segregated blank filters (10, 4 and 5 for NJU, PAES and NUIST, respectively) and 35 daily blank $PM_{2.5}$ filters (25, 6 and 9 for NJU, PAES and NUIST, respectively) were obtained at the three sites. All the blank filters were put in the samplers without inlet air flow for 24 h when the field campaigns finished. We took NJU as an example to check the consistency between the two types of samplers. As shown in Figure S3 in the supplement, excellent agreement was found between the mass concentrations of $PM_{1.8}$ collected with quartz fiber in MOUDI impactor and $PM_{2.5}$ collected with TH-150 sampler.

Three anions (SO_4^{2-}, NO_3^- and Cl^-) and five cations (Na^+, NH_4^+, K^+, Mg^{2+}, and

163 Ca^{2+}) in particles were measured in the extracted solution of the filter samples with

164 ion chromatography (Dx-120, Dionex Ltd., USA). CS12A column (Dionex Ltd.) with

165 20 mM MSA eluent and AS11-HC column (Dionex Corp.) with 8 mM KOH eluent

166 were used to measured cations and anions, respectively (Chen et al., 2019). Elemental

167 carbon (EC) and organic carbon (OC) were measured with an OC-EC aerosol

168 analyzer (Sunset Inc., USA) following the thermal-optical transmittance (TOT)

169 protocol. In addition to thermal EC and OC, the instrument also provides the optical

170 EC and OC by measuring the light attenuation (ATN). As the ATN is determined not

171 only by EC but also by BrC, the optical method may overestimate EC and

172 underestimate OC (Cui et al., 2016; Massabò et al., 2016). The optical EC and OC

173 were thus not adopted in this work. More details on the analyzer operation were

174 described in our previous studies (Chen et al., 2017; 2019). We used the methanol

175 soluble organic carbon (MSOC) as BrC surrogate. It was believed to be more suitable

176 than water soluble organic carbon (WSOC), as a large fraction of BrC absorption

177 comes from OC insoluble in water (Cheng et al., 2016; 2017; Huang et al., 2018; Lei

178 et al., 2018). The analytical procedure was described in details in Chen et al. (2019).

179 As shown in Figure S4 in the supplement, MSOC was measured to account for 88%

180 of the total OC mass for all the samples in this work, similar to the fraction of 85% by

181 Cheng et al. (2016). Elements of size-resolved particles collected in the Teflon filters

182 (As, Al, Ba, Cd, Co, Cr, Cu, Fe, Mn, Mo, Ni, Ti, V, and Zn) were measured with an

183 inductively coupled plasma-mass spectrometer (ICP-MS, PerkinElmer ELAN 9000,

184 USA) in order to provide further information on the aerosol sources. More detailed

185 information on the instrument was provided by Khan et al. (2016) including the

186 precision, calibration, detection limit, and analytical procedures.

187

188 **2.3 Measurements of real time aerosol scattering coefficients**

189   The aerosol scattering coefficients were measured using two different types of

190 integrating nephelometers. Two Model Aurora 1000G nephelometers (Ecotech Pty

191 Ltd, Australia) were operated at NJU and PAES at the wavelength of 520 nm, and one

192 Model 3563 nephelometer (TSI Inc., USA) was operated at NUIST at the wavelength

of 550 nm. To obtain the dry aerosol scattering coefficient, the three nephelometers controlled the RH of the inflow air under 50% by the heated inlet to mitigate the impact of water vapor on the scattering coefficient. The nephelometers at NJU and PAES were operated at a flow rate of 5 L/min, and that at NUIST was at 20 L/min. Routine maintenance including zero calibration and span check was conducted following the instrument manual.

To explore the RH impact on aerosol light scattering, an online monitoring instrument Cavity Attenuated Phase Shift Albedo monitor (CAPS, Shoreline Science Research Inc., Japan) was used to measure the ambient scattering coefficient at NJU in real ambient conditions. The instrument operates at the wavelength of 530 nm (Onasch et al., 2015; Petzold et al., 2013), and more details on its operation during the campaigns were provided by Chen et al. (2019).

2.4 Data analysis

2.4.1 Estimation of the scattering coefficient of aerosol chemical species with different methods

The details of IMPROVE1999 and IMPROVE2007 are summarized in the Supplement Section A1. Neglecting the light-absorbing effect of BrC, the two algorithms could overestimate the scattering coefficient of OM (Yan et al., 2014). The major difference between the two versions is that the IMPROVE2007 algorithm considers the variety of mass scattering efficiencies due to particle size for $(NH_4)_2SO_4$, NH_4NO_3 and OM. With consideration of the BrC presence, we conducted the multiple linear regression between the measured light scattering components and aerosol scattering coefficient with SPSS 16.0 (Cheng et al., 2011; Tian et al., 2016) to obtain the mass scattering efficiency (MSE). The contributions of sea salt and soil dust were excluded by subtracting their light scattering coefficients from the measured $PM_{2.5}$ one. The $PM_{2.5}$ scattering coefficient can then be estimated statistically based on the concentrations of individual chemical species as Eq. (1):

$$
\begin{aligned}
b_{sca} = &\ a \times f_S(RH)[Small\ (NH_4)_2SO_4] + b \times f_L(RH)[Large\ (NH_4)_2SO_4] \\
&+ c \times f_S(RH)[Small\ NH_4NO_3] + d \times f_L(RH)[Large\ NH_4NO_3] \\
&+ e \times ([Small\ OM] - m \times [Small\ MSOC]) \\
&+ f \times ([Large\ OM] - n \times [Large\ MSOC])
\end{aligned}
\tag{1}
$$

where b_{sca} is the measured PM$_{2.5}$ scattering coefficient excluding the contribution of sea salt and soil dust; a, c and e are the MSEs of $(NH_4)_2SO_4$, NH_4NO_3 and OM (except for light-absorbing BrC) in the small size mode, respectively; b, d and f are the MSEs of $(NH_4)_2SO_4$, NH_4NO_3 and OM (except for light-absorbing BrC) in the large size mode, respectively (definitions of small and large size modes for various aerosol components can be referred to Pitchford et al. (2007)); m and n indicate the mass fractions of light-absorbing BrC to total MSOC in small and large modes, respectively (definitions of small and large size modes of MSOC are the same as other species); $f(RH)$ (including $f_L(RH)$ and $f_S(RH)$) of sulfate and nitrate indicate the scattering hygroscopic growth factor under a given relative humidity (RH), obtained from Pitchford et al. (2007).

In addition to PM$_{2.5}$, the scattering coefficient for particles at a given size ($b_{sca}(RH)$) is calculated with the Mie theory (Bohren et al., 1998; Cheng et al., 2015):

$$
b_{sca}(RH) = \int \pi [D_p \times \frac{g(RH)}{2}]^2 \times Q_{sca}[m(RH),\ Dp,\ \lambda] \times N(D_p) \times g(RH)dD_p
\tag{2}
$$

where $m(RH)$ is the aerosol refractive index; $g(RH)$ is the hygroscopic growth factor; Q_{sca} is the scattering efficiency for a single spherical particle with diameter D_p and can be calculated with the Mie theory by inputting D_p, $m(RH)$ and the incident wavelength (λ); $N(D_p)$ is the number concentration of particle with diameter D_p. In general, three typical models are proposed to represent the particle mixing state including internal, external and core-shell mixture (Jacobson, 2001; Seinfeld and Pandis, 2006). The methods of calculating the parameters including $m(RH)$ and $N(D_p)$ are different for the three mixed states, and the details can be referred to Ding et al. (2015).

2.4.2 Source apportionment of aerosol scattering coefficients with a coupled model of PMF and Mie theory

Positive matrix factorization (PMF) is an effective technology for source

248   apportionment of atmospheric aerosols (Kim and Hopke, 2004). PMF does not require

249   the source profile (i.e., the aerosol chemistry speciation by source category) as a

250   model input, and thus excludes the uncertainty of source profiles which were

251   commonly developed based on literatures or measurements across the country in

252   China. In this study, PMF 5.0 software was applied for the source apportionment of

253   accumulated mode particles. In total, 245, 145 and 163 aerosol samples were analyzed

254   at NJU, PAES and NUIST, respectively. It is currently difficult to resolve the sources

255   of secondary organic aerosol (SOA) with PMF. In this study, a simplified method was

256   applied to differentiate the sources of primary and secondary aerosols. Organic carbon

257   is split into primary and secondary organic carbon (POC and SOC), and the SOC

258   concentration was calculated with the EC-tracer method (Chen et al., 2017). The

259   source contributions of primary particles were obtained using the PMF model, and

260   those of secondary inorganic aerosol (SIA) and SOA were further determined based

261   on estimates of the nitrogen oxides (NO_x), sulfur dioxide (SO_2) and volatile organic

262   compounds (VOCs) emissions in a local inventory (Huang, 2018; Lang et al., 2017;

263   Wang et al., 2015). The chemical components applied in the PMF model included

264   inorganic ions, carbonaceous components and metallic elements. We followed the

265   method described in the PMF manual and Tian et al. (2016) to calculate the chemical

266   component uncertainties in the measurement dataset. Criteria including the optimum

267   number of factors and the minimization of an objective function Q were determined

268   based on the principles described in previous studies (Moon et al., 2008; Tian et al.,

269   2016; Watson et al., 2015) and applied in the model to obtain the best PMF solution.

270   A coupled model combining PMF and the Mie theory was developed to evaluate

271   the sources of aerosol light scattering. The procedure of the method was as follows: (1)

272   the EPA-PMF model was applied to quantify the contributions of different sources to

273   the mass concentrations of chemical species in size-segregated particles; (2) the

274   contribution (%) of the ith chemical component to the aerosol scattering coefficient at

275   size D_p was estimated based on Mie theory; (3) the percentage contribution (%) of the

276   i^{th} component in the jth source category to the total scattering at size D_p was calculated

277   as the product of the percentage contribution (%) of the ith chemical species to the

278 total scattering and that of the jth source category to the mass concentration of the ith

279 species in the particles at size D_p, as indicated in Eq.(3); and (4) the percentage

280 contribution (%) of the jth source to the total scattering at size D_p was estimated by

281 summing η_{ijD_p}, as shown in Eq. (4).

282 $$\eta_{ijDp} = a_{ijDp} \cdot \frac{b_{iDp}}{\sum\limits_{i=1}^{m} b_{iDp}} \times 100\% \qquad (3)$$

283 $$\eta_{jD_p} = \sum_{i=1}^{I} \eta_{ijD_p} \qquad (4)$$

284 where i and j stand for the numbers of aerosol chemical components and potential

285 sources, respectively; η_{ijDp} (%) is the contribution (%) of ith scattering component in

286 the jth source to the total particle scattering at size D_p; η_j (%) is the contribution (%) of

287 the jth source to the total scattering at size D_p; a_{ijDp} is the relative contribution (%) of

288 the jth source to the ith chemical component in particles with size D_p from PMF

289 modeling; and b_{iDp} is the contribution of the ith chemical component to the total

290 scattering from Mie modeling.

3 RESULTS AND DISCUSSION

291

3.1 Mass concentrations and size distributions of PM compositions

292

293 Based on the national definition on ambient Air Quality Index (AQI) (MEP,

294 2012), we divided the whole sampling period into three categories, i.e., the clean

295 period with AQI less than 100, the lightly polluted period with AQI between 100 and

296 200, and the heavily polluted period with AQI above 200. Note that the AQI is a

297 unitless index calculated based on the daily concentrations of regulated air pollutants

298 including NO_2, SO_2, CO, O_3, $PM_{2.5}$ and PM_{10} (MEP, 2012). As summarized in Table 1,

299 the average daily $PM_{2.5}$ mass concentrations at the three conditions were calculated at

300 47.9 ± 15.8, 102.1 ± 16.4, and 163.1 ± 13.6 μg/m^3, respectively. The mass

301 concentration of secondary inorganic ions (SO_4^{2-}, NO_3^- and NH_4^+) for the heavily

302 polluted period was 4.4 and 2.2 times those for the clean and lightly polluted periods,

303 respectively. The corresponding values for the carbonaceous aerosols (the sum of OC

and EC) were 3.1 and 1.9 times, respectively, and the OC to EC ratios increased from 4.5 for the clean period to 5.2 for the heavy period. In addition to the particulate components, gaseous pollutants such as NO_2 and SO_2 were also significantly elevated from the clean to the heavy periods. These results imply that secondary aerosol formation was an important source of enhanced $PM_{2.5}$ for the heavily polluted period.

Figure S5 in the Supplement compares the size distributions of mass concentrations for particles and selected chemical components under three pollution levels. Bimodal size distributions were found for PM and OC mass concentrations, with the two peaks at the ranges of 0.56-1.0 μm and 3.2-5.6 μm, respectively. This bimodal pattern could partly result from the coexistence of primary and secondary sources of OC. POC with larger sizes may contribute largely to the peak in the coarser particles. In contrast, due to chemistry reactions of biogenic and anthropogenic VOCs, SOC was expected to be abundant in the accumulation mode (0.18-1.8 μm) (Cao et al., 2007). The size distributions of NO_3^- and SO_4^{2-} followed a unimodal distribution with the mass concentrations peak at the range of 0.56-1.0 μm, as most of the inorganic aerosols were generated through secondary formation. The mass concentrations of PM, NO_3^-, SO_4^{2-} and OC for all sizes were enhanced from the clean to the polluted periods, and the biggest differences were found in the size bin of 0.56-1.0 μm. As shown in Figure S5a, the concentrations of $PM_{0.56-1.0}$ for the heavily and lightly pollution periods were 7.0 and 2.7 times greater than that for the clean period, respectively. Moreover, $PM_{0.56-1.0}$ contributed 31%, 23%, and 15% to the total mass concentrations of particles for the heavily, lightly polluted and clean periods, respectively, implying that the enhanced concentration of $PM_{0.56-1.0}$ was an important reason for the aggravated pollution. As shown in Figure S5b-S5d, the sum of NO_3^-, SO_4^{2-} and OC for the heavily polluted period was 2.9 and 10.7 times greater than those for the lightly polluted and clean periods, respectively. From clean to heavily polluted periods, the collective mass fraction of the three components to $PM_{0.56-1.0}$ increased from 42% to 64%. The results indicated that the increased NO_3^-, SO_4^{2-} and OC at the size bin of 0.56-1.0 μm could be an indicator for the serious air pollution events. As indicated in Table 1, moreover, SNA was elevated more than OC in the heavily

polluted period compared to the clean days. During the heavily polluted episodes in winter, enhancement of SO_4^{2-} and NO_3^- could be more significant than OM because the high relative humidity and precursor emissions promoted the generation of SNA (Tian et al., 2014). During clean periods (commonly in summer), NH_4NO_3 would dissociate to NH_3 and HNO_3 at high temperature, while the SOC concentration might increase due to the high levels of O_3 and solar radiation. Similar result was found in Beijing, where the mass fraction of SNA was observed to increase from 19% on non-haze days to 31% on haze days, while that of OM decreased from 38% to 31% (Tian et al., 2016).

To explore the mass fractions of major chemical species in the particles, the PM mass was reconstructed as $(NH_4)_2SO_4$ ($1.38\times SO_4^{2-}$), NH_4NO_3 ($1.29\times NO_3^-$), OM ($1.55\times OC$), fine soil (FS) and EC (Cheng et al., 2015; Pitchford et al., 2007). As shown in Figure S6 in the Supplement, strong correlations were found between the reconstructed PM mass concentrations and the measurements for $PM_{1.8}$ ($R^2=0.91$) and PM_{10} ($R^2=0.89$) at the three sites. The slope of $PM_{1.8}$ (0.85) was greater than that of PM_{10} (0.72), indicating smaller unidentified fraction in the $PM_{1.8}$. The larger unidentified mass in the reconstructed PM_{10} was probably due to underestimation in the crustal components (Hueglin et al., 2005).

Figure 1 presents the mass concentrations and fractions of the reconstructed aerosol chemical species by particle size under the three pollution levels. NH_4NO_3, $(NH_4)_2SO_4$, and OM were the dominant components in particles. From the clean to heavily polluted periods, their mass fractions to $PM_{1.8}$ increased from 16.9 to 35.3%, from 14.9 to 28.6% and from 16.7 to 22.2%, respectively (Figure 1b, Figure 1d and Figure 1f). The mass fraction of OM in $PM_{1.8}$ was 5.4% and 7.4% larger than NH_4NO_3 and $(NH_4)_2SO_4$ for the clean period, while 13.3% and 6.6% smaller than those for the heavily polluted period, respectively. The results further confirmed that substantial growth in the mass of NH_4NO_3 and $(NH_4)_2SO_4$ was an important reason for the aerosol pollution. The formation of sulfate, nitrate, and ammonium (SNA) is mainly affected by the emissions of precursors and the atmospheric oxidation capacity Due to the great use of fossil fuel consumption, the emissions of precursors SO_2 and

NO$_X$ per unit area in eastern China were estimated 2.3 and 3.4 times larger than the national average, respectively (Cheng et al., 2012; Shi et al., 2014). Under high RH, moreover, the SNA formation could significantly be elevated through gas-to-particle heterogeneous reactions for the heavily polluted period (Seinfeld and Pandis, 2006). Sulfate mass concentration, for example, increased from 6.4 μg/m^3 for the clean period to 53.3 μg/m^3 for the heavily polluted period. Among all the size bins, NH$_4$NO$_3$ and (NH$_4$)$_2$SO$_4$ were estimated to contribute the most to the mass concentrations for 0.56-1.0 μm particles, with their mass fraction ranging 19.4-39.7% and 18.1-34.7%, respectively, across different pollution levels. In comparison, the largest contributions of OM appeared in the 0.056-0.18 μm fraction and were 31.2%, 29.0% and 52.3% for the clean, lightly polluted and heavily polluted periods, respectively. As the largest PM fraction was found in the 0.56-1.0 μm size bin for the heavily pollution period, the elevated concentrations of NH$_4$NO$_3$ and (NH$_4$)$_2$SO$_4$ in PM$_{0.56-1.0}$ were the major causes of the increased aerosol pollution.

Figure S7 in the Supplement compares the size distributions of PM mass concentrations and selected chemical species at the three sites. As mentioned above, a bimodal distribution with two peaks at 0.56-1.0 μm and 3.2-5.6 μm was observed for PM and OC at all the three sites, attributed to the coexistence of primary and secondary sources. Different from PAES and NUIST, NO$_3^-$ had an obvious small coarse mode peak at NJU. Previous studies suggested that the chemistry of coarse mode NO$_3^-$ can vary in different locations, and the components include NH$_4$NO$_3$, NaNO$_3$ and Ca(NO$_3$)$_2$ (Pakkanen et al., 1996). As NJU was close to the G25 highway, the reaction of HNO$_3$ with crustal particles could be an important process for coarse mode NO$_3^-$ formation. The highest mean concentrations of NO$_3^-$ and SO$_4^{2-}$ at the 0.56-1.0 μm size among the three sites were observed at NJU, followed by NUIST and PAES. As NO$_3^-$ and SO$_4^{2-}$ were the major components of the aerosol light scattering, the variety of their mass concentrations at 0.56-1.0 μm could be a crucial reason for the visibility difference among the three sites. A greater difference was found for the size distribution of OC among the three sites, and the highest concentration at the 0.56-1.8 μm size was observed at NUIST. Our previous work

394 found that NUIST was greatly influenced by VOCs emissions of surrounding

395 industrial plants (Chen et al., 2019). Given its capability of light scattering and

396 absorption, the abundant OC in the area could play an important role on the visibility.

397 **3.2 Evaluation and optimization of the IMPROVE algorithm**

398 Figure S8 in the Supplement presents the linear regressions between the

399 measured daily aerosol scattering coefficients with nephelometers (b_{sp-m}) and those

400 calculated with IMPROVE algorithms ($b_{sp-1999}$ and $b_{sp-2007}$) based on the measured

401 concentrations of particle components at the three sites. At each site, strong

402 correlations were found between the observation and IMPROVE estimation ($R^2 \geq$

403 0.94), indicating consistency between the different techniques. As shown in Figure

404 S8a, the calculated aerosol scattering coefficients $b_{sp-1999}$ were 30%, 16% and 19%

405 smaller than the measured values at NJU, PAES and NUIST, respectively. Similar

406 results were found for other megacities in eastern China. Based on the online

407 analytical methods, for example, Cheng et al. (2015) estimated that the scattering

408 coefficients predicted by the IMPROVE1999 algorithm were 34% smaller than the

409 measurement for a heavy pollution period in Shanghai. A greater underestimation of

410 the scattering coefficient existed at NJU than the other two sites, partly due to the

411 relatively abundance of sulfate and nitrate in particles at NJU. The sum of SO_4^{2-} and

412 NO_3^- accounted for $35.3 \pm 13.2\%$ of the total mass concentrations of $PM_{2.5}$ at NJU,

413 larger than the fraction at PAES ($27.6 \pm 12.9\%$) and NUIST ($24.1 \pm 11.6\%$) (note the

414 SO_4^{2-} and NO_3^- concentrations at the 0.56-1.0 μm were the largest at NJU as well, as

415 shown in Figure S7). Tao et al. (2014b) and Cheng et al. (2015) suggested that the

416 relatively small MSE of sulfate and nitrate aerosols in the IMPROVE1999 algorithm

417 might result in underestimation of the scattering coefficient in China, as sulfate and

418 nitrate were the main light-scattering components in $PM_{2.5}$.

419 As shown in Figure S8b, $b_{sp-2007}$ was only 4% smaller than the measurement at

420 NJU, and 4% and 18% larger at PAES and NUIST, respectively. Overall, the

421 performance of the IMPROVE2007 algorithm was better than that of the

422 IMPROVE1999, although deviation still existed due to the uncertainty in MSEs for

423 chemical species and the presence of light absorption organic matter such as BrC. A

424 relatively large deviation between b_{sp-m} and $b_{sp-2007}$ was found at NUIST compared to

425 NJU and PAES. Chen et al. (2019) and Shao et al. (2016) found higher annual average

426 concentration of non-methane hydrocarbon at NUIST (34.4 ppbv) than NJU (22.0

427 ppbv) or PAES (27.1 ppbv). The more VOCs in the atmosphere were expected to

428 increase the SOC formation and to result in big deviation of $b_{sp-2007}$, as the OM with

429 light-absorption capability was not considered in IMPROVE2007.

430   Using the optimized IMPROVE algorithm as described in Section 2.4.1, the

431 aerosol scattering coefficients were recalculated and compared against the observation

432 at the three sites, as illustrated in Figure 2. Good correlations were found between the

433 observed and calculated scattering coefficients at all the sites ($R^2 \geq 0.96$), and the

434 regression slopes were estimated to be much closer to 1 than those between

435 observations and predictions with the IMPROVE1999 or IMPROVE2007 algorithms

436 (Figure S8). In addition, the MSEs calculated based on the Mie theory were applied to

437 evaluate the results of the IMPROVE algorithms. As presented in Figure S9 in the

438 Supplement, the MSEs of $(NH_4)_2SO_4$ and NH_4NO_3 calculated with the optimized

439 IMPROVE algorithm were closer to the MSE simulated by Mie theory than those

440 with the IMPROVE2007 algorithm. The results indicated the optimized algorithm had

441 a better performance and could reduce the bias from the US IMPROVE algorithm.

442   As summarized in Table 2, the MSEs estimated with the optimized IMPROVE

443 algorithm were 2.29, 4.82, 2.62, 5.35, 4.46, and 6.41 m^2/g for small sulfate, large

444 sulfate, small nitrate, large nitrate, small and large OM, respectively. In comparison,

445 the MSEs for the small and large size modes using the IMPROVE2007 were 2.2 and

446 4.8 m^2/g for $(NH_4)_2SO_4$, respectively, and 2.4 and 5.1 m^2/g for NH_4NO_3, respectively.

447 The slightly larger MSEs from the optimized IMPROVE algorithm for $(NH_4)_2SO_4$ and

448 NH_4NO_3 implied underestimation of the scattering coefficients of inorganic

449 components when applying the previous algorithm. There were clear differences in

450 the MSEs of OM (especially for fine OM) between the two algorithms, resulting from

451 consideration of the light-absorbed OM in the optimized algorithm. Indicated by the

452 m values in Table 2, the light-absorbed OC accounted for 66% and 71% of the fine

MSOC mass at NJU and PAES, respectively, indicating that most of the fine MSOC had only light-absorption capacity. Unlike NJU and PAES, less than half of the fine MSOC (39%) had light-absorption capacity at NUIST, likely resulting from the varied sources of OM at the three sites. As described in our previous study (Chen et al., 2019), substantial OC was from the secondary formation in industrial polluted region, and its light-absorption capacity was weaker than that from the primary emissions.

In this study, the optimized IMPROVE algorithm for $PM_{2.5}$ did not include the contribution of sea salt or soil dust. As illustrated in Figure S10 in the supplement, sea salt and soil dust accounted collectively for less than 10% of the total $PM_{2.5}$ scattering coefficient, suggesting that the two species should have limited impact on the IMPROVE algorithm optimization. In order to be concise in the optimized formula and to ensure the stability of the multiple linear regression, therefore, only $(NH_4)_2SO_4$, NH_3NO_3 and OM were used as independent variables. Through field measurement and data reconstruction in different cities, previous studies explored the concentrations of $PM_{2.5}$ and its chemical components for various cities in China (Chen et al., 2019; Feng et al., 2012; Lai et al., 2016; Tao et al., 2013., Yang et al., 2011; Zhao et al., 2013). The major components of light scattering in aerosols, SNA, were found to typically account for half of the $PM_{2.5}$ mass concentrations in eastern Chinese cities like Nanjing, Shanghai, and Jinan (Yang et al., 2011). Given the similar SNA levels and strong regional transport of pollution among those cities, the optimized IMPROVE algorithm applied in Nanjing in this work is believed to be more suitable than the previous algorithms for eastern China. Moreover, for other regions with rapidly developing economy and fast industrialization in China including Beijing-Tianjin-Hebei or Pearl River Delta regions, the current work provides methodology and data support for the studies of aerosol light scattering in cities with relatively serious aerosol pollution. Given the fast changes in emission control and aerosol pollution in those regions, more campaigns on aerosol optical and chemical properties are recommended to further evaluate and improve the applicability of the optimized IMPROVE algorithm.

3.3 Effects of mixing state and relative humidity on aerosol light scattering

Figure 3 presents the scattering coefficients measured by nephelometer and those simulated by Mie theory at the three sites under dry conditions (RH < 40%). The simulated scattering coefficients based on the assumption of an external mixing state were larger than those based on core-shell and internal mixing states at all the three sites. Compared with the internal and core-shell states, the simulated scattering coefficients in the external mixing state were closer to the measurements at NJU and PAES (Figure 3a and 3b), indicating the reasonable assumption of external mixtures as the main mixing state of particles. Similarly, Ma et al. (2012) also suggested that the external mixture was an important particle mixing state in northern China based on a stochastic particle-resolved aerosol box model. Assuming the aerosol components were externally mixed, Cheng et al. (2015) estimated the MSEs of aerosol species in Shanghai, and found better agreement between the optimized scattering coefficients and the measurements. At NUIST, the measured scattering coefficients were closer to the simulated values in internal and core-shell states, likely due to the high aging level of SOA at the industrial site (Figure 3c). Due to the strong atmospheric oxidation and thereby the abundance of SOA coatings at NUIST, our previous study suggested that the aerosol aging process could result in the growth of internally mixed BC (Chen et al., 2019). Based on the observation of O_3 and percentage of internally mixed BC, Lan et al. (2013) suggested that photochemical production of secondary aerosol components was the main reason for the switching from an external mixing state to an internal mixing state for BC.

In an actual environment, ambient aerosols are typically hygroscopic under the conditions of high RH, and it is an important reason for visibility degradation. Table S1 in the Supplement summarizes the growth factors (GF) of particle size measured in Nanjing at different RH levels in previous studies. To evaluate the rationality of those GF values, we followed the method by Tao et al. (2014b) and calculated the scattering hygroscopic growth factor (f(RH)) at NJU based on the measured ambient scattering coefficients by CAPS and the dry scattering coefficients by nephelometer, as shown in Figure S11 in the Supplement. The correlation between f(RH) and RH was fitted

513   through the power regression. Figure S12 in the Supplement presents a good

514   agreement between the scattering coefficients estimated by f(RH) and those obtained

515   by the Mie theory (R^2=0.95). The results indicate the accuracy of the GF values

516   applied on different particle sizes and RH levels. The estimated and measured

517   scattering coefficients at NJU under ambient condition are shown in Figure S13 in the

518   Supplement. Different from the estimation under the dry conditions, the lowest value

519   was found for the externally mixing state among the three mixing modes. In the

520   externally mixing state, only sulfate and nitrate particles had hygroscopicity under wet

521   conditions, whereas each particle had the capability of hygroscopic growth in the

522   internal mixing and core-shell states, resulting in a significant increment in the

523   scattering coefficient. Similarly, comparing the measured scattering coefficients under

524   the dry and ambient conditions (Figure 3 and Figure S13), the simulated values based

525   on an external mixing state were closer to the measurements than the other two modes,

526   implying that RH had a limited effect on the particle mixing state.

527   To explore the impact of RH on the light scattering of particles with different

528   sizes, the size distribution of f(RH) was estimate and shown in Figure 4. Large

529   differences were found between f(RH) when the RH was above and below 75%, and

530   high RH enhanced the capacity of scattering hygroscopicity growth of small size

531   particles. Approximately 140 nm particles had strong hygroscopicity when the RH

532   was below 75%, whereas a high f(RH) (1.41±0.03) was observed for the

533   accumulation mode particles from 100 to 400 nm when the RH was above 75%.

534   Similar results were reported for Beijing: larger hygroscopic GF was measured for

535   accumulation mode particles (100–300 nm) with a hygroscopicity tandem differential

536   mobility analyzer (H-TDMA), consistent with the elevated abundance of the

537   light-scattering compositions such as sulfate and nitrate (Meier et al., 2009).

538

539   **3.4 Size distribution of aerosol light scattering by pollution level**

540   Figure 5 shows the size distribution of the scattering coefficients for particles and

541   given chemical components under the three pollution levels, based on the

542   measurements at all the three sites. Note the result was obtained with Mie theory

under the assumption of external mixing at ambient condition. Although other mixing states might be more important at specific site (e.g., internal mixing at NUIST), their influence on scattering coefficient estimation was modest (Figure 3). The scattering coefficients of particles for all size categories were the largest for the heavily polluted period (Figure 5a). The accumulation mode particles (0.18-1.8 μm) accounted for 92.9%, 92.6 and 93.4% of the total scattering coefficients for the clean, lightly polluted and heavily polluted periods, respectively. In particular, particles in the size bin of 0.56-1.0 μm accounted for 57% and 63% of the scattering coefficient for the heavily and lightly polluted periods, respectively, much larger than that for the clean period, 38%. From the results of Section 3.1, the abundance of particles of different sizes was considered to be an important factor for the variety of scattering coefficients across the whole size range.

As the dominant chemical components of aerosol light scattering, $(NH_4)_2SO_4$, NH_4NO_3 and OM collectively contributed 90%, 76% and 60% to the mass concentrations of $PM_{0.56-1.0}$ for the heavily polluted, lightly polluted and clean periods, respectively (Figure S5b-S5d). The scattering coefficients of $(NH_4)_2SO_4$ and NH_4NO_3 were the largest in the size bin of 0.56-1.0 μm for the three pollution levels, and their contributions increased along with the aggravation of pollution (Figure 5b and Figure 5c). The OM concentration in the size bin of 0.56-1.0 μm was 2.5 μg/m^3 for the clean period, and those for the lightly and heavily polluted periods were 160% and 510% larger, respectively. The scattering coefficient of OM in the size bin of 0.56-1.0 μm for the heavily polluted period was 15% less than that for the lightly polluted period, indicating the more important role of OM in the particle scattering effect for the lightly polluted period (Figure 5d). The large OM scattering contribution could likely be explained by the elevated mass fraction of OM and/or enhancement of the OM MSE. It could be inferred that the low visibility during heavy pollution resulted mainly from the enhancement of the scattering effect of SNA.

The MSEs of given chemical components in $PM_{1.8}$ are presented by pollution level in Figure 6. Increased MSEs for $(NH_4)_2SO_4$ and NH_4NO_3 were found along with the elevated $PM_{2.5}$ pollutions (Figure 6a). The large contributions of inorganic

components and their strong light scattering ability were important reason for the reduced visibility during the heavily polluted period. Although the largest OM concentrations were observed in each size bin for the heavy pollution period, the smallest MSE of OM in $PM_{1.8}$ was found for the heavily polluted period (3.73 m^2/g, Figure 6b). As discussed in Section 3.2, most of the fine MSOC was expected to have only a light-absorption effect whereas large MSOC had light-scattering capability. With the optimized IMPROVE algorithm, the mass fraction of light-absorption OC to total MSOC mass was estimated at 66.9±5.8% for the heavily polluted period, much larger than those for clean and lightly polluted periods at 44.3±6.5% and 50.8±5.9%, respectively, as shown in Figure S14 in the Supplement. Therefore, the small MSE of OM for the heavily polluted period was partly attributed to the abundance of light absorption BrC in $PM_{2.5}$.

For the whole research period, the MSEs of $(NH_4)_2SO_4$, NH_4NO_3 and OM in $PM_{1.8}$ were calculated at 3.95, 4.26 and 4.14 m^2/g with the Mie theory, while the analogue numbers in $PM_{2.5}$ were 3.94, 4.31 and 5.25 with the optimized IMPROVE algorithm, respectively (Table 2). Very good agreement between the two methods was found for SNA, and clearer discrepancy existed for OM, indicating a larger uncertainty in the evaluation of organic aerosol scattering.

3.5 Source apportionment of aerosol light scattering with the PMF-Mie coupled model

As illustrated in Figure 5, the light scattering of the accumulation mode (0.18-1.8 μm) accounted for the largest proportion of the total light scattering. To better understand the causes of visibility degradation, the source apportionment of aerosol light scattering at this size range was conducted for different pollution levels with the PMF and Mie coupled model, as described in Section 2.4.2. The PMF model was adopted to identify the potential sources and to estimate their respective contributions to the mass concentration of accumulation mode particles. To resolve the appropriate number of factors, different numbers of identifiable sources were tested. The source profiles and contributions to accumulation mode particles at the three sites are

603   presented in Figure S15 in the Supplement and Figure 7a-c, respectively. The main

604   sources identified at the three sites include coal combustion, industrial pollution,

605   vehicle, fugitive dust, biomass burning, and SIA (Figure S15). Compared to NJU and

606   NUIST, vehicle contributed more to accumulated particles at the urban site PAES

607   (Figure 7b). As stated in Section 2.4, we assumed that the contribution of the

608   individual source category to the secondary particle component was proportional to

609   the fraction of that source category to the emissions of corresponding precursors

610   (Lang et al., 2017). Based on the emission inventory of precursors of SOC (VOCs)

611   and SIA (NO_x, SO_2 and NH_3) in Nanjing (Huang, 2018), the source apportionment for

612   primary and secondary particles of accumulation mode at the three sites were

613   estimated, and the results are presented in Tables S2-S4 in the Supplement. With the

614   source apportionment of secondary components, the contributions of coal combustion

615   and industrial pollution increased 45-50% and 138-478% compared to those for

616   primary particles across the three sites, respectively. The result indicates that the

617   gaseous precursors from coal combustion and industrial pollution greatly elevate the

618   aerosol pollution.

619   The contributions of different aerosol species to the aerosol light scattering were

620   estimated using the Mie model, and the results are presented in Table S5 in the

621   Supplement. OM contributed the most to the total scattering at the three sites (31%,

622   29% and 33% for NJU, PAES and NUIST, respectively). Compared to other Chinese

623   mega cities, the contribution of OM in Nanjing was close to that for inland cities like

624   Beijing (Tao et al., 2015) and Tianjin (Wang et al., 2016b), but was much larger than

625   that observed in a coastal megacity, Guangzhou (Tao et al., 2014c).

626   Combined with the source apportionment from the PMF model, Figure 7d-7f

627   illustrates the source contribution to aerosol light scattering at the three sites. Coal

628   combustion, industrial plants and vehicle were the major sources of the aerosol light

629   scattering in Nanjing, and the three source categories collectively accounted for

630   64-70% of the total scattering capacity of aerosols. Given their relatively intensive

631   activities in urban and industrial regions, vehicles and industrial plants were identified

632   as the largest contribution sources at PAES and NUIST, respectively. Indicated by the

22

633 dashed lines in Figure 7d-7f, the collective contributions of secondary aerosol

634 components were estimated to be 26.7%-35.2% of the total scattering at the three sites,

635 suggesting the important role of secondary aerosol formation in visibility reduction.

636   Figure 8 illustrates the source apportionment of aerosol light scattering for the

637 clean and polluted periods at the three sites. Coal combustion contributed the most to

638 the total scattering for the clean period, and the contribution declined significantly for

639 the polluted period, from 39% to 21%, from 38% to 19% and from 35% to 18% at

640 NJU, PAES and NUIST, respectively. The results implied that coal combustion might

641 not be the most important reason for visibility degradation in polluted periods.

642 Similarly, the contribution of fugitive dust during the polluted period was estimated to

643 be smaller than that for the clean condition. In contrast, the contributions of vehicles

644 and industrial pollution to light scattering increased from 27% to 48%, from 27% to

645 47% and from 31% to 62% for the polluted periods compared to the clean period at

646 NJU, PAES, and NUIST, respectively. As shown in Figure 8b and 8c, particularly, the

647 contribution of primary emissions from vehicles to aerosol scattering was estimated to

648 increase from 11.4% to 21.5% at PAES, and that from industrial plants increased from

649 4.5% to 13.5% at NUIST. The primary aerosol emissions from vehicles and industrial

650 plants were thus identified as the main cause of visibility reduction in the urban and

651 industrial areas, respectively. Similarly, Wang et al. (2016b) suggested that vehicle

652 was the dominate source of aerosol light extinction in Hangzhou, with the

653 contribution to the total extinction coefficient of $PM_{2.5}$ reaching 30.2%. The present

654 study indicated that more effective measures for reducing the primary particle

655 emissions from vehicles and industrial production should be conducted to avoid

656 severe haze pollution in urban and industrial regions.

657   In addition, the results suggest that secondary aerosols were another important

658 contributor to the reduced visibility. From the clean to the heavily polluted periods, as

659 shown in Figure 8, the contributions of secondary aerosols to the total light scattering

660 increased from 19.9% to 36.7%, from 20.9% to 32.4%, and from 28.6% to 41.7% at

661 NJU, PAES, and NUIST, respectively. As shown in Table 3, the contributions of SIA

662 to the total scattering at the three sites were ranged at 14.5%-19.9% and 24.5%-28.0%,

663   much more than those of SOA at 4.1%-8.7% and 7.9%-13.7% for the clean and

664   polluted periods, respectively. The results imply that SIA had a greater impact on

665   visibility degradation. Although the contribution of coal combustion to the total

666   scattering declined from clean to polluted periods, the contributions of SIA from coal

667   combustion for the polluted periods were 88%, 35% and 36% larger than those for the

668   clean period at NJU, PAES and NUIST, respectively. The enhancement of SIA from

669   coal combustion was thus an important cause of polluted days. Moreover, the

670   contribution of SOA to the total scattering coefficient during the polluted periods was

671   estimated at 13.7% at NUIST, larger than the 7.9% and 9.1% at PAES and NJU,

672   respectively, indicating that the contribution of SOA to visibility reduction at

673   industrial polluted areas should not be ignored. Notably, there is uncertainty in the

674   methodology of source apportionment of aerosol scattering coefficients. In particular,

675   the assumption that the secondary components were proportional to the emissions of

676   their precursors is a simplified method and probably led to large bias, as the

677   complicated nonlinear mechanism of secondary aerosol formation is not recognized.

678   To further reduces the uncertainty and to improve the source apportionment, some

679   specific tracers of secondary aerosols like semi-volatile and low-volatile

680   oxygen-containing organic aerosols can be observed with advanced technology such

681   as aerosol mass spectrometry (AMS), and the observation data can then be combined

682   with the receptor models to quantify the source contribution of secondary aerosols.

683   Besides, air quality model that integrates particle source apportionment technology

684   (PSAT) is recommended to be applied to evaluate and confirm the performance of the

685   source apportionment of secondary aerosols with the receptor model.

686   **4 CONCLUSIONS**

687   A comprehensive investigation of the light-scattering properties of atmospheric

688   aerosols was conducted from November 2015 to March 2017 at three functional sites

689   in Nanjing. High concentrations of sulfate and nitrate in $PM_{0.56-1.0}$ were the major

690   causes of the heavy particle pollution events. The varied abundance of secondary

691   inorganic components at the three sites was an important reason for the visibility

692 differences, and OC played an important role on the visibility reduction in the

693 industrial area due to its complicated optical effect. Based on the measured aerosol

694 scattering coefficients and the mass concentrations of aerosol components, an

695 optimized algorithm of IMPROVE that considered the light absorption effect of OM

696 was developed to better represent the aerosol optical property.

697   Compared with internal and core-shell mixing states, the simulated scattering

698 coefficients based on an external mixing assumption were closer to the measurements

699 at NJU and PAES, indicating that externally mixed particles widely existed at urban

700 and suburban areas. At the industrial site NUIST, the high aging level of SOA was the

701 main reason for particle switching from external to internal mixing states. The results

702 for the scattering coefficients under dry and ambient conditions indicated that RH had

703 little effect on particle mixing state but a large impact on the scattering coefficients.

704 Particles in the size range of 0.56-1.0 μm contributed the most (38%-63%) to the total

705 scattering coefficient under different pollution levels. As the dominant light scattering

706 species in aerosols, NH_4NO_3, $(NH_4)_2SO_4$ and OM collectively contributed 90%, 81%

707 and 76% of the mass concentrations of $PM_{0.56-1.0}$ for the heavily polluted, lightly

708 polluted and clean periods, respectively. The low visibility during the heavy pollution

709 period mainly resulted from the enhanced light scattering of SNA. The abundance of

710 light-absorption OC was an important reason for the relatively low contribution of

711 OM to light scattering in the heavy pollution period.

712   Through a coupled model of PMF and Mie theory, we found coal combustion,

713 industrial plants and vehicle were the main sources of the visibility reduction in

714 Nanjing. Vehicles and industrial plants were the main causes for visibility reduction in

715 urban and industrial areas, respectively. The increased emissions of SIA precursors

716 from coal combustion were an important cause of polluted days, and the contribution

717 of SOA to visibility reduction at industrial pollution areas should not be ignored. The

718 source apportionment of aerosol light scattering in this work provides scientific

719 evidence for the control of haze pollution in different functional areas of cities in

720 developed eastern China.

721

DATA AVAILABILITY

All data in this study are available from the authors upon request.

AUTHOR CONTRIBUTIONS

DC developed the strategy and methodology of the work and wrote the draft. YZ improved the methodology and revised the manuscript. JZ, HY and XY provided observation data of aerosol scattering coefficient.

COMPETING INTERESTS

The authors declare that they have no conflict of interest.

ACKNOWLEDGEMENT

REFERENCES

Alexander, D. T. L., Crozier, P. A., Anderson, J. R.: Brown carbon spheres in East Asian outflow and their optical properties, Science, 321, 833-836, doi:10.1126/science.1155296, 2008.

Andreae, M. O., Schmid, O., Yang, H., Chand, D., Yu, J. Z., Zeng, L. M., Zhang, Y. H.: Optical properties and chemical composition of the atmospheric aerosol in urban Guangzhou, China, Atmos. Environ., 42, 6335-6350, doi:10.1016/j.atmosenv.2008.01.030, 2008.

Bohren, C. F, Huffman, D. R.: Absorption and scattering of light by small particles [R], New York: Wiley, Inc., 1998.

Bond, T. C., Bergstrom, R. W.: Light Absorption by Carbonaceous Particles: An

Investigative Review, Aerosol Sci. Technol., 40, 27-67, doi:10.1080/02786820500421521, 2006.

Cao, J. J., Lee, S. C., Chow, J. C., Watson, J. G., Ho, K. F., Zhang, R. J., Jin, Z. D., Shen, Z. X., Chen, G. C., Kang, Y. M., Zou, S. C., Zhang, L. Z., Qi, S. H., Dai, M. H., Cheng, Y., Hu, K.: Spatial and seasonal distributions of carbonaceous aerosols over China, J. Geophys. Res., 112, D22S11, doi:10.1029/2006JD008205, 2007.

Cao, J. J., Wang, Q. Y., Chow, J. C., Watson, J. G., Tie, X. X., Shen, Z. X., Wang, P., An, Z. S.: Impacts of aerosol compositions on visibility impairment in Xi'an, China, Atmos. Environ., 59, 559-566, doi:10.1016/j.atmosenv.2012.05.036, 2012.

Chen, D., Cui, H., Zhao, Y., Yin, L., Lu, Y., Wang, Q.: A two-year study of carbonaceous aerosols in ambient $PM_{2.5}$ at a regional background site for western Yangtze River Delta, China, Atmos. Res., 183, 351-361, doi:10.1016/j.atmosres.2016.09.004, 2017.

Chen, D., Zhao, Y., Lyu, R., Wu, R., Dai, L., Zhao, Y., Chen, F., Zhang, J., Yu, H., Guan, M.: Seasonal and spatial variations of optical properties of light absorbing carbon and its influencing factors in a typical polluted city in Yangtze River Delta, China, Atmos. Environ., 199, 45-54, doi:10.1016/j.atmosenv.2018.11.022, 2019.

Cheng, M. C., You, C. F., Cao, J., Jin, Z.: Spatial and seasonal variability of water soluble ions in PM2.5 aerosols in 14 major cities in China, Atmos. Environ., 60, 182-192, 10.1016/j.atmosenv.2012.06.037, 2012.

Cheng, S. H., Yang, L. X., Zhou, X. H., Xue, L. K., Gao, X. M., Zhou, Y., and Wang, W. X.: Size-fractionated water-soluble ions, situ pH and water content in aerosol on hazy days and the influences on visibility impairment in Jinan, China, Atmos. Environ., 45, 4631–4640, doi:10.1016/j.atmosenv.2011.05.057, 2011.

Cheng, Y., He, K.B., Du, Z.Y., Engling, G., Liu, J.M., Ma, Y.L., Zheng, M., Weber, R.J.: The characteristics of brown carbon aerosol during winter in Beijing, Atmos. Environ., 127, 355-364, doi:10.1016/j.atmosenv.2015.12.035, 2016.

Cheng, Y., He, K.B., Engling, G., Weber, R., Liu, J.M., Du, Z.Y., Dong, S.P.: Brown and black carbon in Beijing aerosol: Implications for the effects of brown coating on light absorption by black carbon, Sci. Total Environ., 599–600, 1047-1055.

778   doi:10.1016/j.scitotenv.2017.05.061, 2017.

779   Cheng, Z., Jiang, J., Chen, C., Gao, J., Wang, S., Watson, J.G., Wang, H., Deng, J.,

780   Wang, B., Zhou, M.: Estimation of aerosol mass scattering efficiencies under high

781   mass loading: case study for the megacity of Shanghai, China, Environ. Sci. Technol.,

782   49, 831-838, doi:10.1021/es504567q, 2015.

783   Cui, X., Wang, X., Yang, L., Chen, B., Chen, J., Andersson, A., Gustafsson, Ö.:

784   Radiative absorption enhancement from coatings on black carbon aerosols, Sci. Total

785   Environ., 551-552, 51-56, doi:10.1016/j.scitotenv.2016.02.026, 2016.

786   Ding, J., Han, S., Zhang, Y., Feng, Y., Wu, J., Shi, G., Wang, J.: Chemical

787   characteristics of particles and light extinction effects in winter in Tianjin, Res.

788   Environ. Sci., 28, 1353-1361, doi:10.13198/j.issn.1001-6929.2015.09.03, 2015.

789   Feng, J. L., Sun, P., Hu, X. L., Zhao, W., Wu, M. H., Fu, J. M.: The chemical

790   composition and sources of $PM_{2.5}$ during the 2009 Chinese New Year's holiday in

791   Shanghai, Atmos. Res., 118, 435-444, doi:10.1016/j.atmosres.2012.08.012, 2012.

792   Huang, R. J., Yang, L., Cao, J., Chen, Y., Chen, Q., Li, Y., Duan, J., Zhu, C., Dai, W.,

793   Wang, K.: Brown Carbon Aerosol in Urban Xi'an, Northwest China: The Composition

794   and Light Absorption Properties, Environ. Sci. Technol., 52, 6825-6833,

795   doi:10.1021/acs.est.8b02386, 2018.

796   Huang, Y.W: Effects of changes in emission and meteorological conditions on fine

797   particulate levels in the city scale, Master thesis, Nanjing University, 2018.

798   Hueglin, C., Gehrig, R., Baltensperger, U., Gysel, M., Monn, C., and Vonmont, H.:

799   Chemical characterisation of $PM_{2.5}$, PM_{10} and coarse particles at urban, near-city

800   and   rural   sites   in   Switzerland,   Atmos.   Environ.,   39,   637–651,

801   doi:10.1016/j.atmosenv.2004.10.027, 2005.

802   Jacobson, M.Z.: Strong radiative heating due to the mixing state of black carbon in

803   atmospheric aerosols, Nature, 409, 695-697, doi:10.1038/35055518, 2001.

804   Khan, M. F., Latif, M. T., Hwa, S. W., Amil, N., Nadzir, M. S. M., Sahani, M., Tahir,

805   N. M., Jing, X. C.: Fine particulate matter in the tropical environment: monsoonal

806   effects, source apportionment, and health risk assessment, Atmos. Chem. Phys., 16,

807   597-617, doi:10.5194/acp-16-597-2016, 2016.

Kim, E., Hopke, P.K.: Improving source identification of fine particles in a rural northeastern US area utilizing temperature-resolved carbon fractions, J. Geophys. Res.: Atmos., 109, D09204, doi:10.1029/2003jd004199, 2004.

Lai, S.C.: Characterization of PM2.5 and the major chemical components during a 1-year campaign in rural Guangzhou, Southern China, Atmos. Res., 167, 208-215, doi:10.1016/j.atmosres.2015.08.007, 2016.

Lan, Z. J., Huang, X. F., Yu, K. Y., Sun, T. L., Zeng, L. W., Hu, M.: Light absorption of black carbon aerosol and its enhancement by mixing state in an urban atmosphere in South China, Atmos. Environ., 69, 118-123, doi:10.1016/j.atmosenv.2012.12.009, 2013.

Lang, J. L., Cheng, S. Y., Wen, W., Liu, C., Wang, G.: Development and application of a new $PM_{2.5}$ source apportionment approach, Aerosol Air Qual. Res., 17, 340-350, doi: 10.4209/aaqr.2015.10.0588, 2017.

Lei, Y., Shen, Z., Wang, Q., Zhang, T., Cao, J., Sun, J., Zhang, Q., Wang, L., Xu, H., Tian, J., 2018. Optical characteristics and source apportionment of brown carbon in winter PM2.5 over Yulin in Northern China, Atmos. Res., 213, 27-33, doi:10.1016/j.atmosres.2018.05.018, 2018.

Li, B., Zhang, J., Zhao, Y., Yuan, S., Zhao, Q., Shen, G., Wu, H.: Seasonal variation of urban carbonaceous aerosols in a typical city Nanjing in Yangtze River Delta, China, Atmos. Environ., 106, 223-231, doi:10.1016/j.atmosenv.2015.01.064, 2015.

Liu, X., Cheng, Y., Zhang, Y., Jung, J., Sugimoto, N., Chang, S. Y., Kim, Y. J., Fan, S., Zeng, L.: Influences of relative humidity and particle chemical composition on aerosol scattering properties during the 2006 PRD campaign, Atmos. Environ., 42, 1525-1536, doi:10.1016/j.atmosenv.2007.10.077, 2008.

Liu, H. J., Zhao, C. S., Nekat, B., Ma, N., Herrmann, H.: Aerosol hygroscopicity derived from size-segregated chemical composition and its parameterization in the North China Plain, Atmos. Chem. Phys., 14, 2525-2539, doi:10.5194/acp-14-2525-2014, 2014.

Liu, D., Whitehead, J., Alfarra, M. R., Reyesvillegas, E., Spracklen, D. V., Reddington, C. L., Kong, S., Williams, P. I., Ting, Y. C., Haslett, S.: Black-carbon absorption

enhancement in the atmosphere determined by particle mixing state, Nature Geosci., 10, 184-188, doi:10.1038/ngeo2901, 2017.

Lowenthal, D. H., Naresh, K.: PM2.5 mass and light extinction reconstruction in IMPROVE, J. Air Waste Manag. Assoc., 53, 1109-1120, doi:10.1080/10473289.2003.10466264, 2003.

Ma, N., Zhao, C. S., Müller, T., Cheng, Y. F., Liu, P. F., Deng, Z. Z., Xu, W. Y., Ran, L., Nekat, B., Van Pinxteren, D., Gnauk, T., Müller, K., Herrmann, H., Yan, P., Zhou, X.J., Wiedensohler, A.: A new method to determine the mixing state of light absorbing carbonaceous using the measured aerosol optical properties and number size distributions, Atmos. Chem. Phys., 12, 2381-2397, doi:10.5194/acp-12-2381-2012, 2012.

Malm, W.C., Hand, J. L.: An examination of the physical and optical properties of aerosols collected in the IMPROVE program, Atmos. Environ., 41, 3407-3427, doi:10.1016/j.atmosenv.2006.12.012, 2007.

Massabò, D., Caponi, L., Bove, M.C., Prati, P.: Brown carbon and thermal-optical analysis: A correction based on optical multi-wavelength apportionment of atmospheric aerosols, Atmos. Environ., 125, 119-125, doi:10.1016/j.atmosenv.2015.11.011, 2016.

Meier, J., Wehner, B., Massling, A., Birmili, W., Nowak, A., Gnauk, T., Bruggemann, E., Herrmann, H., Min, H., Wiedensohler, A.: Hygroscopic growth of urban aerosol particles in Beijing (China) during wintertime: a comparison of three experimental methods, Atmos. Chem. Phys., 9, 6865-6880, doi:10.5194/acp-9-6889-2009, 2009.

Ministry of Environmental Protection of China (MEP): Technical regulation on ambient air quality index, China Environ.Sci. Press, HJ633-2012, 2012.

Moon, K. J., Han, J. S., Ghim, Y. S., Kim, Y. J.: Source apportionment of fine carbonaceous particles by positive matrix factorization at Gosan background site in East Asia, Environ. Int., 34, 654-664, doi:10.1016/j.envint.2007.12.021, 2008.

Onasch, T. B., Massoli, P., Kebabian, P. L., Hills, F. B., Bacon, F. W., Freedman, A.: Single Scattering Albedo Monitor for Airborne Particulates, Aerosol Sci. Technol., 49, 267-279, doi:10.1080/02786826.2015.1022248, 2015.

868 Pakkanen, T. A., Kerminen, V. M., Hillamo, R. E., Makinen, M., Makela, T., and

869 Virkkula, A.: Distribution of nitrate over seasalt and soil derived particles implications

870 from a field study, J. Atmos. Chem., 24, 189–205, 1996.

871 Petzold, A., Onasch, T., Kebabian, P., Freedman, A.: Intercomparison of a Cavity

872 Attenuated Phase Shift-based extinction monitor (CAPS PMex) with an integrating

873 nephelometer and a filter-based absorption monitor, Atmos. Meas. Tech., 6,

874 1141-1151, doi:10.5194/amt-6-1141-2013, 2013.

875 Pitchford, M., Malm, W., Schichtel, B., Kumar, N., Lowenthal, D., Hand, J.: Revised

876 algorithm for estimating light extinction from IMPROVE particle speciation data, J.

877 Air Waste Manag. Assoc., 57, 1326-1336, doi:10.3155/1047-3289.57.11.1326, 2007.

878 Ramanathan, V., Li, F., Ramana, M. V., Praveen, P. S., Kim, D., Corrigan, C. E.,

879 Nguyen, H., Stone, E. A., Schauer, J. J., Carmichael, G. R., Adhikary, B., Yoon, S. C.:

880 Atmospheric brown clouds: Hemispherical and regional variations in long-range

881 transport, absorption, and radiative forcing, J. Geophys. Res.: Atmos., 112, D22S21,

882 doi:10.1029/2006JD008124, 2007.

883 Schwartz, S.: The Whitehouse Effect–Shortwave radiative forcing of climate by

884 anthropogenic aerosols: An overview, J. Aerosol Sci., 27, 359–382,

885 doi:10.1016/0021-8502(95)00533-1, 1996.

886 Seinfeld, J. H., Pandis.: Atmospheric chemistry and physics: From air pollution to

887 climate change, doi:10.1080/00139157.1999.10544295, 2006.

888 Shao, P., An, J., Xin, J., Wu, F., Wang, J., J, D., Wang, Y.: Source apportionment of

889 VOCs and the contribution to photochemical ozone formation during summer in the

890 typical industrial area in the Yangtze River Delta, China, Atmos. Res., 176-177, 64-74,

891 doi:10.1016/j.atmosres.2016.02.015, 2016.

892 Shi, Y., Chen, J., Hu, D., Wang, L., Yang, X., Wang, X.: Airborne submicron

893 particulate (PM1) pollution in Shanghai, China: chemical variability,

894 formation/dissociation of associated semi-volatile components and the impacts on

895 visibility, Sci. Total Environ., 473, 199-206, 10.1016/j.scitotenv.2013.12.024, 2014.

896 Swietlicki, E., Hansson, H. C., Hämeri, K., Svenningsson, B., Massling, A.,

897 McFiggans, G., McMurry, P. H., Petäjä, T., Tunved, P., Gysel, M., Topping, D.,

Weingartner, E., Baltensperger, U., Rissler, J., Wiedensohler, A., Kulmala, M.: Hygroscopic properties of submicrometer atmospheric aerosol particles measured with H-TDMA instruments in various environments – a review, Tellus B, 60, 432–469, doi:10.1111/j.1600-0889.2008.00350.x, 2008.

Tang, I. N.: Chemical and size effects of hygroscopic aerosols on light scattering coefficients, J. Geophys. Res.: Atmos., 101, 19245-19250, doi:10.1029/96jd03003, 1996.

Tao, J., Cheng, T., Zhang R.: Chemical composition of PM2.5 at an urban site of Chengdu in southwestern China, Adv. Atmos. Sci., 30, 1070-1084, doi:10.1007/s00376-012-2168-7, 2013.

Tao, J. C , Zhao, C. S., Ma, N., Liu, P. F.: The impact of aerosol hygroscopic growth on the single-scattering albedo and its application on the NO_2 photolysis rate coefficient, Atmos. Chem. Phys., 14, 12055-12067, doi:10.5194/acp-14-12055-2014, 2014a.

Tao, J., Zhang, L., Cao, J., Hsu, S. C., Xia, X., Zhang, Z., Lin, Z., Cheng, T., Zhang, R.: Characterization and source apportionment of aerosol light extinction in Chengdu, southwest China, Atmos. Environ., 95, 552-562, doi:10.1016/j.atmosenv.2014.07.017, 2014b.

Tao, J., Zhang, L., Kinfai, H. O., Zhang, R., Lin, Z., Zhang, Z., Lin, M., Cao, J., Liu, S., Wang, G.: Impact of $PM_{2.5}$ chemical compositions on aerosol light scattering in Guangzhou - the largest megacity in South China, Atmos. Res., 135-136, 48-58, doi:10.1016/j.atmosres.2013.08.015, 2014c.

Tao. J., Zhang, L., Gao. J., Wang. H., Chai. F., Wang. S: Aerosol chemical composition and light scattering during a winter season in Beijing, Atmos. Environ., 110, 36-44, doi:10.1016/j.atmosenv.2015.03.037, 2015.

Tian, S. L., Pan, Y. P., Liu, Z., Wen, T., and Wang, Y. S.: Size-resolved aerosol chemical analysis of extreme haze pollution events during early 2013 in urban Beijing, China, J. Hazard. Mater., 279, 452–460, doi:10.1016/j.jhazmat.2014.07.023, 2014.

Tian, S. L., Pan, Y. P., Wang, Y. S.: Size-resolved source apportionment of particulate matter in urban Beijing during haze and non-haze episodes, Atmos. Chem. Phys., 16,

928   1-19, doi:10.5194/acp-16-1-2016, 2016.

929   Titos, G., Cazorla, A., Zieger, P., Andrews, E., Lyamani, H., Granados-Muñoz, M. J.,

930   Olmo, F. J., Alados-Arboledas, L.: Effect of hygroscopic growth on the aerosol

931   light-scattering coefficient: A review of measurements, techniques and error sources,

932   Atmos. Environ., 141, 494-507, doi:10.1016/j.atmosenv.2016.07.021, 2016.

933   Wang, H., An, J., Cheng, M., Shen, L., Zhu, B., Li, Y., Wang, Y., Duan, Q., Sullivan,

934   A., Xia, L.: One year online measurements of water-soluble ions at the industrially

935   polluted town of Nanjing, China: Sources, seasonal and diurnal variations,

936   Chemosphere, 148, 526-536, doi:10.1016/j.chemosphere.2016.01.066, 2016a.

937   Wang. J., Zhang, Y., Feng, Y., Zheng, X., Li, J., Hong, S., Shen, J., Tan, Z., Jing, D.,

938   Qi, Z.: Characterization and source apportionment of aerosol light extinction with a

939   coupled model of CMB-IMPROVE in Hangzhou, Yangtze River Delta of China,

940   Atmos. Res., 178-179, 570-579, doi:10.1016/j.atmosres.2016.05.009, 2016b.

941   Wang, S. R., Yu, Y. Y., Wang, Q. G., Lu, Y., Yin, L. N., Zhang, Y. Y., Lu, X. B.: Source

942   apportionment of $PM_{2.5}$ in Nanjing by PMF, China Environ.Sci., 35, 3535-3542, 2015.

943   Watson, J. G.: Visibility: Science and regulation, J. Air Waste Manage. Assoc., 52,

944   628-713, 2002.

945   Watson, J. G., Chow, J. C., Lowenthal, D. H., L-W, A. C., Stephanie, S., Edgerton, E.

946   S., Blanchard, C. L.: $PM_{2.5}$ source apportionment with organic markers in the

947   Southeastern Aerosol Research and Characterization (SEARCH) study, J. Air Waste

948   Manage. Assoc., 65, 1104-1118, doi:10.1080/10962247.2015.1063551, 2015.

949   Xu, J., Bergin, M. H., Yu, X., Liu, G., Zhao, J., Carrico, C. M., Baumann, K.:

950   Measurement of aerosol chemical, physical and radiative properties in the Yangtze

951   delta region of China, Atmos. Environ., 36, 161-173,

952   doi:10.1016/s1352-2310(01)00455-1, 2002.

953   Xu, J., Tao, J., Zhang, R., Cheng, T., Leng, C., Chen, J., Huang, G., Li, X., Zhu, Z.:

954   Measurements of surface aerosol optical properties in winter of Shanghai, Atmos.

955   Res., 109-110, 25-35, doi:10.1016/j.atmosres.2012.02.008, 2012.

956   Xue, L., Ding, A., Gao, J., Wang, T., Wang, W., Wang, X., Lei, H., Jin, D., Qi, Y.:

957   Aircraft measurements of the vertical distribution of sulfur dioxide and aerosol

scattering coefficient in China, Atmos. Environ., 44, 278-282, doi:10.1016/j.atmosenv.2009.10.026, 2010.

Yan, C. Q., Zheng, M., Zhang, Y. H.: Research progress and direction of atmospheric brown carbon, Environ. Sci., 35, 4404-4414, doi:10.13227/j.hjkx.2014.11.050, 2014.

Yang, F., Tan, J., Zhao, Q., Du, Z., He, K., Ma, Y., Duan, F., Chen, G., Zhao, Q.: Characteristics of $PM_{2.5}$ speciation in representative megacities and across China, Atmos. Chem. Phys., 11, 5207-5219, doi:10.5194/acp-11-5207-201, 2011.

Zhang, L., Sun, J. Y., Shen, X. J., Zhang, Y. M., Che, H. C., Ma, Q. L., Zhang, Y. W., Zhang, X. Y., Ogren, J. A.: Observations of relative humidity effects on aerosol light scattering in the Yangtze River Delta of China, Atmos. Chem. Phys., 15, 2853-2904, doi:10.5194/acp-15-8439-2015, 2015.

Zhang, Y., Forrister, H., Liu, J., Dibb, J., Anderson, B., Schwarz, J. P., Perring, A. E., Jimenez, J. L., Campuzanojost, P., Wang, Y.: Top-of-atmosphere radiative forcing affected by brown carbon in the upper troposphere, Nature Geosci., 10, doi:10.1038/ngeo2960, 2017.

Zhao, P. S., Dong, F., He, D., Zhao, X. J., Zhang, W. Z., Yao, Q., Liu, H. Y.: Characteristics of concentrations and chemical compositions for PM2.5 in the region of Beijing, Tianjin, and Hebei, China, Atmos. Chem. Phys., 13, 4631-4644. doi:10.5194/acp-13-4631-2013, 2013.

Zhao, Y., Qiu, L. P., Xu, R., Xie, F., Zhang, Q., Y. Yu, Y., Nielsen, C. P., Qin, H., Wang, H., Wu, X., Q. Li, W., Zhang, J.: Advantages of a city-scale emission inventory for urban air quality research and policy: the case of Nanjing, a typical industrial city in the Yangtze River Delta, China, Atmos. Chem. Phys., 15, 12623-12644. doi:10.5194/acpd-15-18691-2015, 2015.

FIGURE CAPTIONS

984 **Figure 1. The mass concentrations and fractions of the main chemical**

985 **components of particles with different sizes in Nanjing on clean, lightly-polluted**

986 **and heavily-polluted days during the sampling period.**

987 **Figure 2. Linear regressions between the measured light scattering coefficients**

988 **and those estimated with the optimized IMPROVE algorithm at NJU, PAES,**

989 **NUIST and all three sites.**

990 **Figure 3. The comparison of measured and estimated dry scattering coefficients**

991 **based on the assumptions of external, internal, and core-shell mixture at NJU (a),**

992 **PAES (b) and NUIST (c).**

993 **Figure 4. The size distribution of hygroscopic scattering growth of particles**

994 **under varied relative humidity levels at the three sites.**

995 **Figure 5. The size distribution of scattering coefficients of aerosol particles (a),**

996 **$(NH_4)_2SO_4$ (b), NH_4NO_3 (c) and OM (d) under different pollution levels. The**

997 **contributions of particles with different sizes to total scattering coefficient are**

998 **indicated in the panels as well.**

999 **Figure 6. The size distribution of mass concentrations of $(NH_4)_2SO_4$, NH_4NO_3 (a),**

1000 **and OM (b) under different pollution levels and mass scattering efficiencies**

1001 **(MSE) for $PM_{1.8}$. The size of dot represents the MSEs of $PM_{1.8}$ (Unit: m^2/g).**

1002 **Figure 7. Source apportionment of accumulation mode particles at NJU (a),**

1003 **PAES (b) and NUIST (c), and source apportionment of light scattering for**

1004 **accumulation mode particles at NJU (d), PAES (e) and NUIST (f). The shadow**

1005 **represents the contribution of secondary aerosols from each source category.**

1006 **Figure 8. Source apportionment of light scattering for accumulation mode**

1007 **particles for the clean and polluted periods at NJU (a), PAES (b) and NUIST (c).**

1008 **The shadow represents the contribution of secondary aerosols from each source**

1009 **category.**

1010

TABLES

Table 1. The concentrations of particulate matter and its chemical components ($\mu g/m^3$), light scattering coefficients (Mm^{-1}), and selected meteorological parameters including wind speed (WS, m/s) and relative humidity (RH, %) at all the three sites for different pollution levels from November 2015 to January 2017.

| Category	Clean period	Lightly polluted period	Heavily polluted period
AQI	65.8 ± 15.7	110.6 ± 21.3	209.4 ± 30.1
PM_{10}	80.4 ± 26.3	143.1 ± 28.6	244.2 ± 21.2
$PM_{2.5}$	47.9 ± 15.8	102.1 ± 16.4	163.1 ± 13.6
OC	8.6 ± 3.2	14.2 ± 3.2	27.6 ± 5.0
EC	1.9 ± 0.9	3.0 ± 1.2	5.3 ± 0.1
SO_4^{2-}	6.9 ± 3.9	13.5 ± 5.6	33.8 ± 9.2
NO_3^-	10.5 ± 5.4	22.7 ± 8.7	47.9 ± 17.7
Cl^-	1.8 ± 1.5	2.2 ± 1.3	4.8 ± 1.4
Ca^{2+}	1.2 ± 0.8	1.3 ± 1.6	0.8 ± 0.1
Na^+	0.8 ± 0.2	0.9 ± 0.3	1.0 ± 0.1
Mg^{2+}	0.1 ± 0.1	0.2 ± 0.1	0.1 ± 0.0
NH_4^+	5.1 ± 1.9	9.2 ± 2.2	16.9 ± 2.5
K^+	0.9 ± 0.2	1.3 ± 0.3	2.1 ± 0.7
CO	0.8 ± 0.2	1.3 ± 0.3	1.6 ± 0.1
NO_2	57.4 ± 18.0	71.6 ± 20.0	91.2 ± 32.8
SO_2	17.7 ± 6.5	21.1 ± 6.0	29.5 ± 12.5
WS	1.6 ± 0.3	1.4 ± 0.5	1.0 ± 0.3
RH	56.1 ± 13.5	62.7 ± 10.8	68.9 ± 4.9
b_{sp}	251.4 ± 170.8	558.3 ± 236.4	1286.2 ± 293.3

Table 2. The mass scattering efficiencies (MSEs, m^2/g) of chemical species in the

optimized and the existing algorithms from the Interagency Monitoring of

Protected Visual Environments (IMPROVE). The sample numbers and the mass

fractions of light-absorption BrC to MSOC for small and large size modes (i.e., *m*

and *n* in Eq.1) are provided for the optimized algorithm.

	Modes	NJU	PAES	NUIST	All the three sites	IMPROVE 2007	IMPROVE 1999
	small	2.32	2.02	2.43	2.29	2.2	-
MSE of $(NH_4)_2SO_4$	large	4.71	4.92	4.86	4.82	4.8	-
	overall	3.91	3.88	4.03	3.94	-	3
	small	2.67	2.48	2.56	2.62	2.4	-
MSE for NH_4NO_3	large	5.37	5.31	5.26	5.35	5.1	-
	overall	4.41	4.13	4.23	4.31	-	3
	small	4.4	4.56	4.22	4.46	2.8	-
MSE of OM	large	6.23	6.36	6.45	6.41	6.1	-
	overall	5.26	5.03	5.35	5.25	-	4
m	-	0.66	0.71	0.39	0.67	-	-
n	-	0.29	0.27	0.33	0.31	-	-
Sample number	-	174	45	63	282	-	-

1024 **Table 3. The source contributions of secondary aerosols to aerosol light**
1025 **scattering at the three sites for the clean and polluted periods (%).**

Air quality level	Sources	NJU		PAES		NUIST	
		SIA	SOA	SIA	SOA	SIA	SOA
Clean	Coal combustion	6.6	0.8	6.5	1.1	7.5	1.3
	Industrial plants	5.8	3.6	4.2	1.5	8.2	6.3
	Vehicles	2.1	1.0	6.1	1.5	4.2	1.1
	Total	19.9		20.9		28.6	
Polluted	Coal combustion	12.4	1.6	8.8	2.3	10.2	2.2
	Industrial plants	10.2	5.8	7.8	3	12.6	9.9
	Vehicles	5.0	1.7	7.9	2.6	5.2	1.6
	Total	36.7		32.4		41.7	

1026

1027   **Figure 1**

1028
1029

1030 **Figure 2**

1031

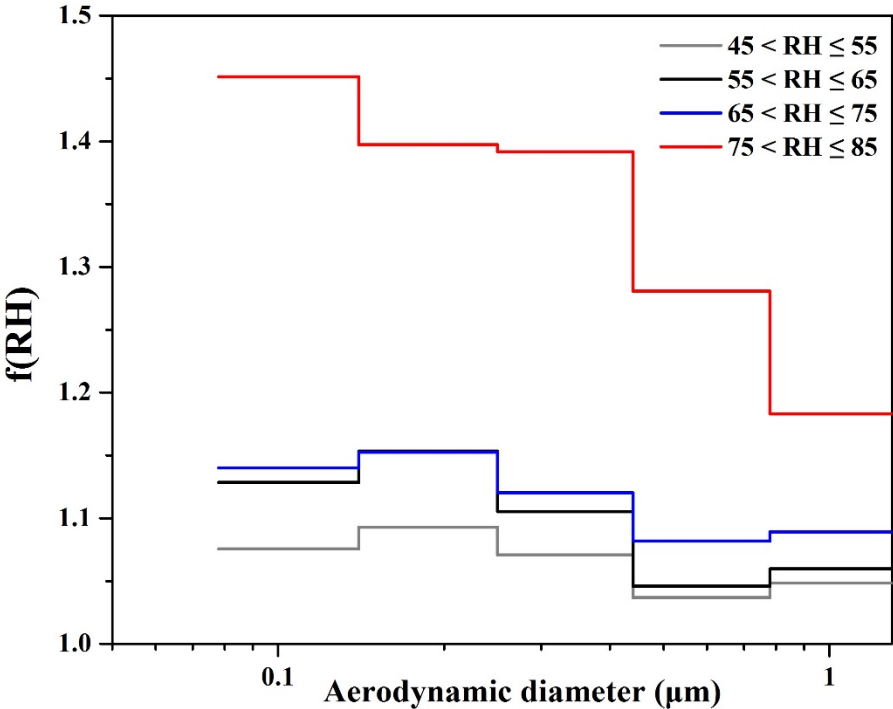1032

1033
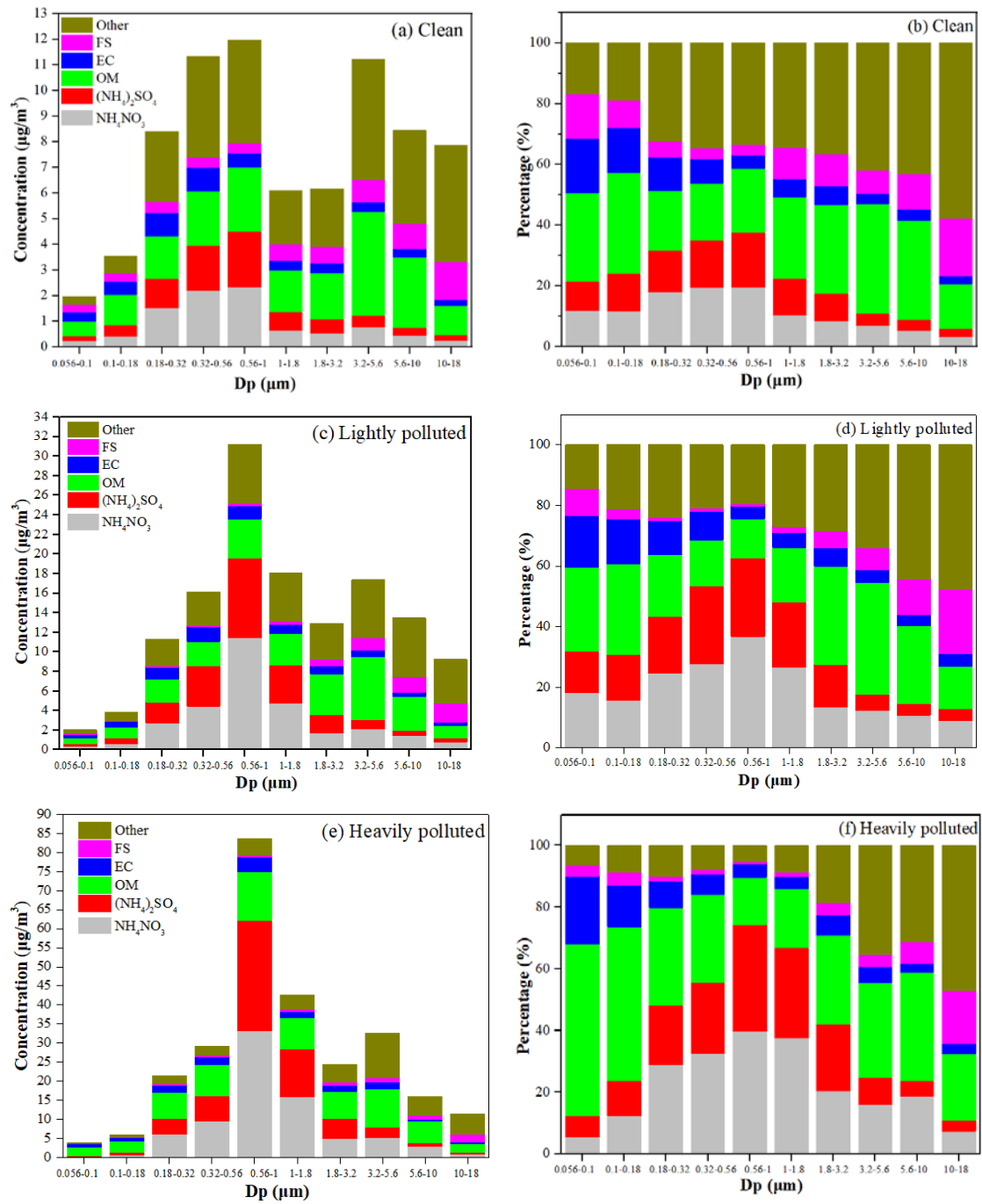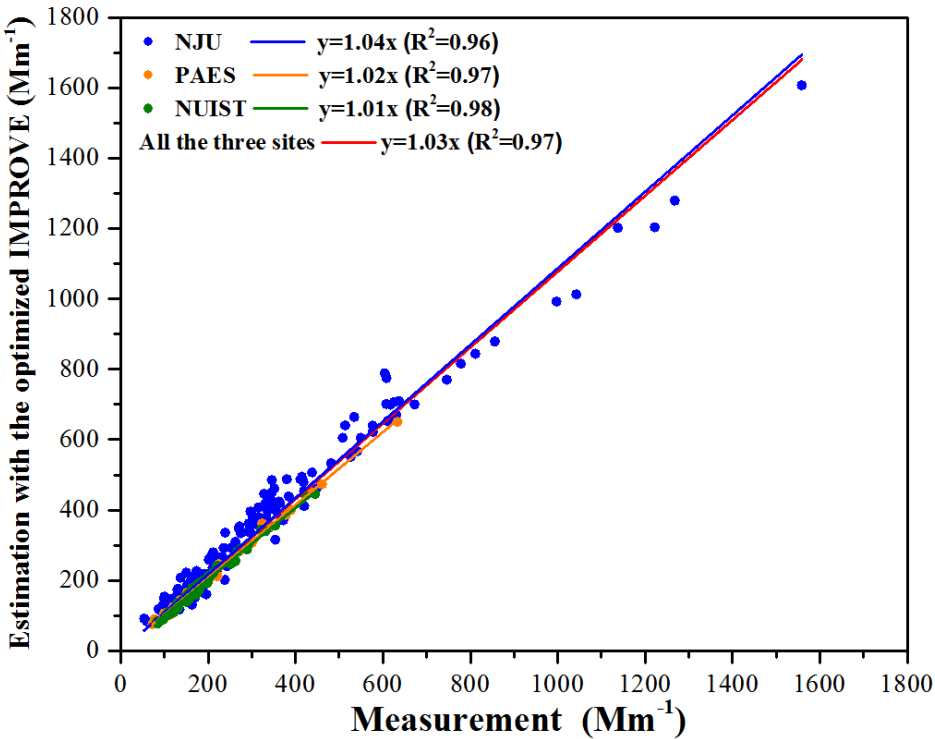
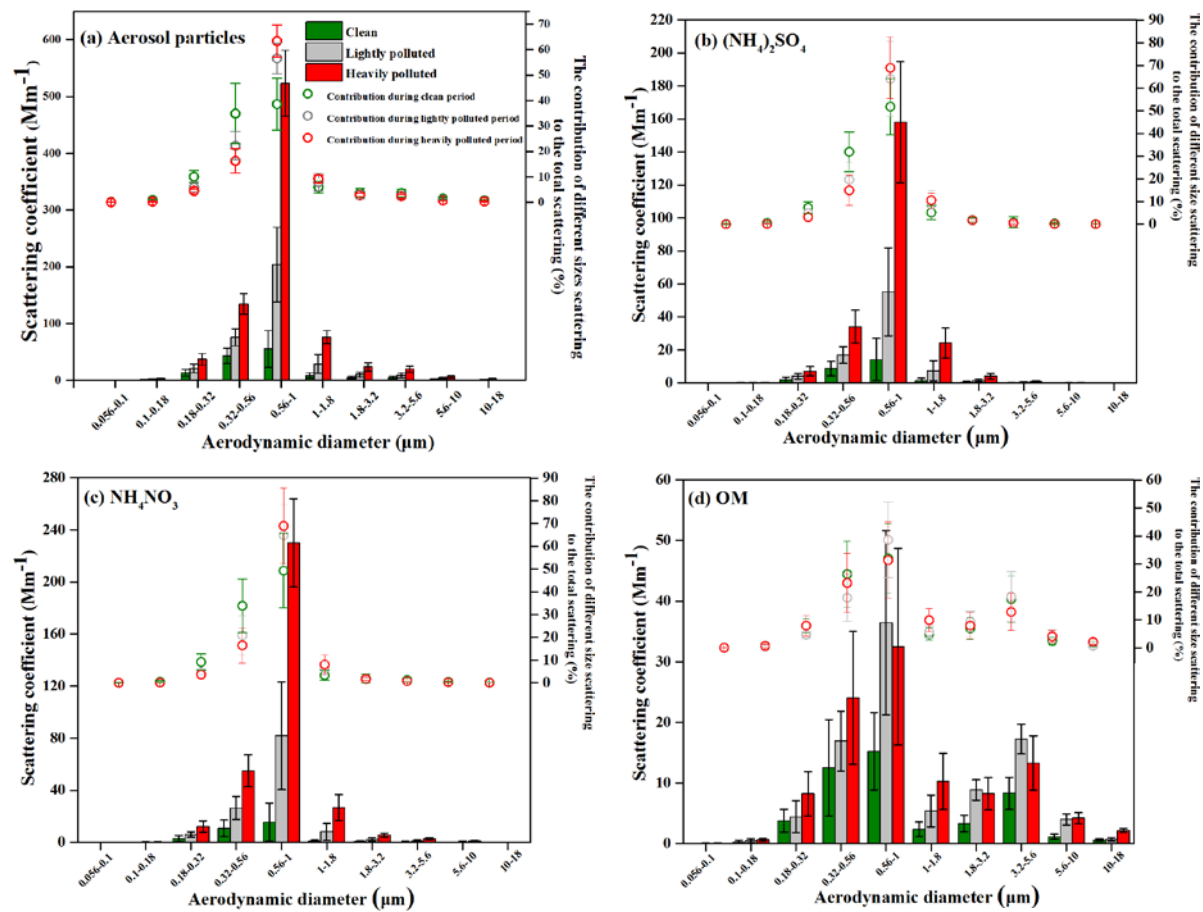1035 **Figure 3**
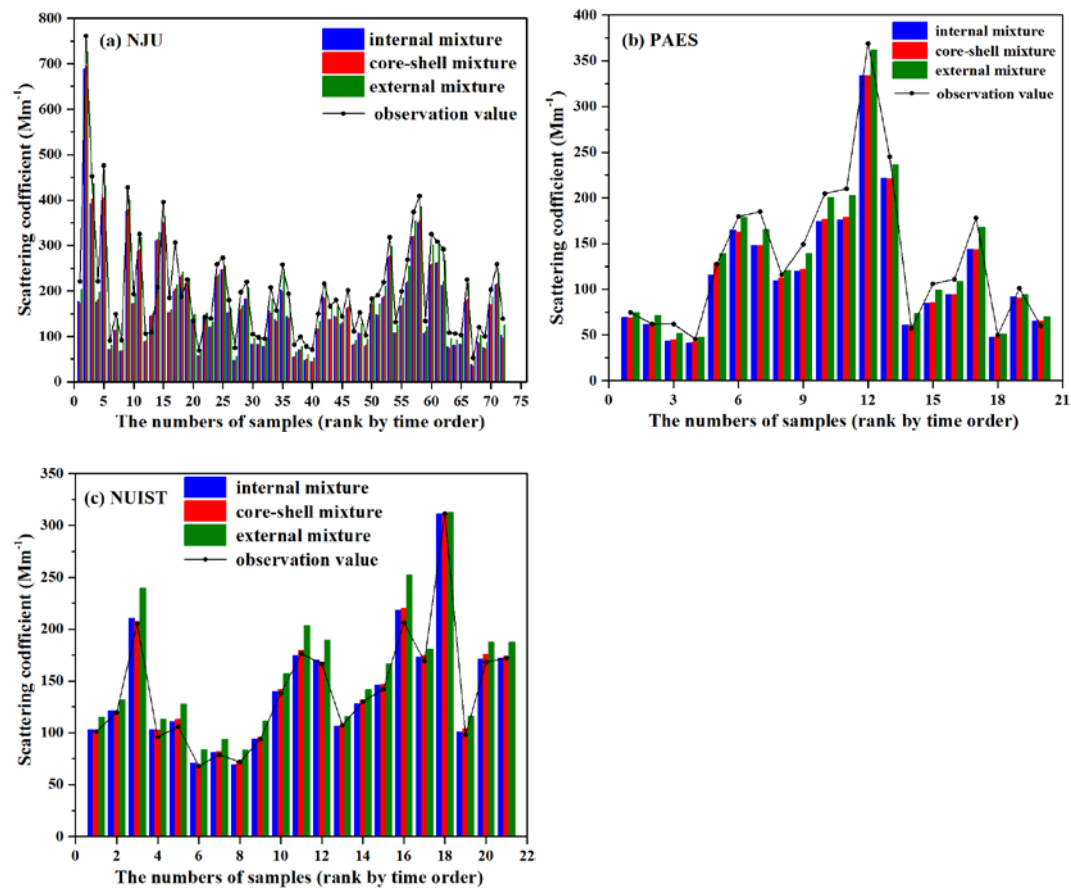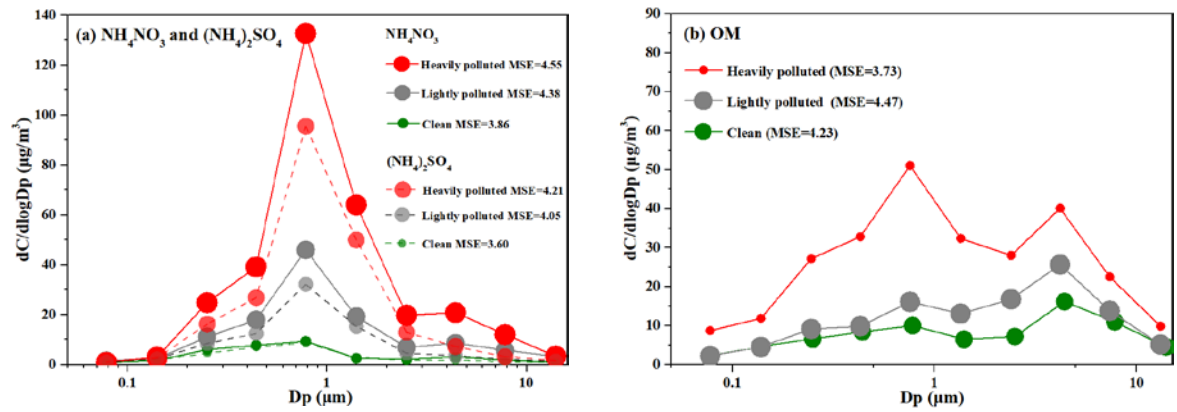

1036

1037

1038   **Figure 4**

1039

1040

1041

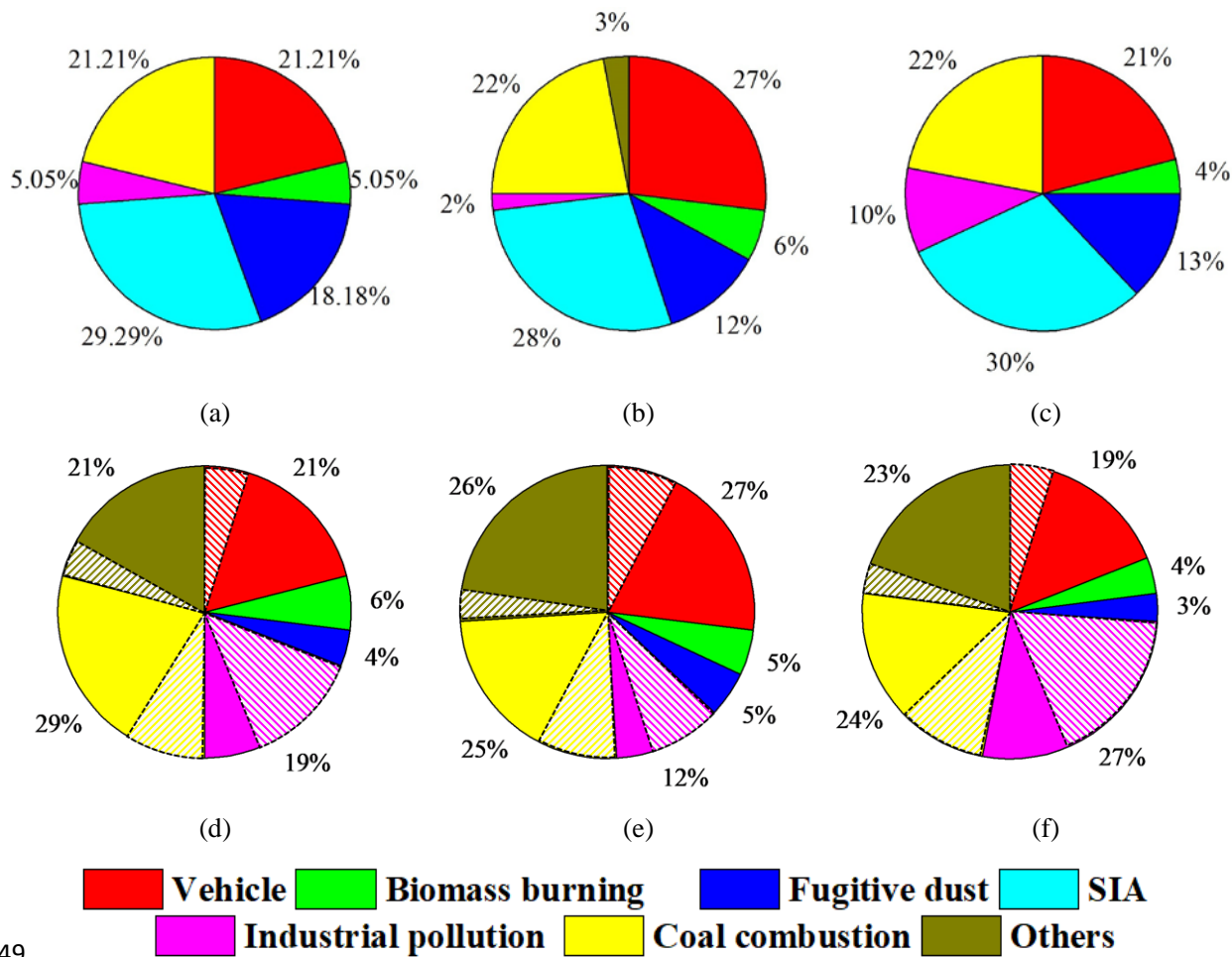1042   **Figure 5**

1043

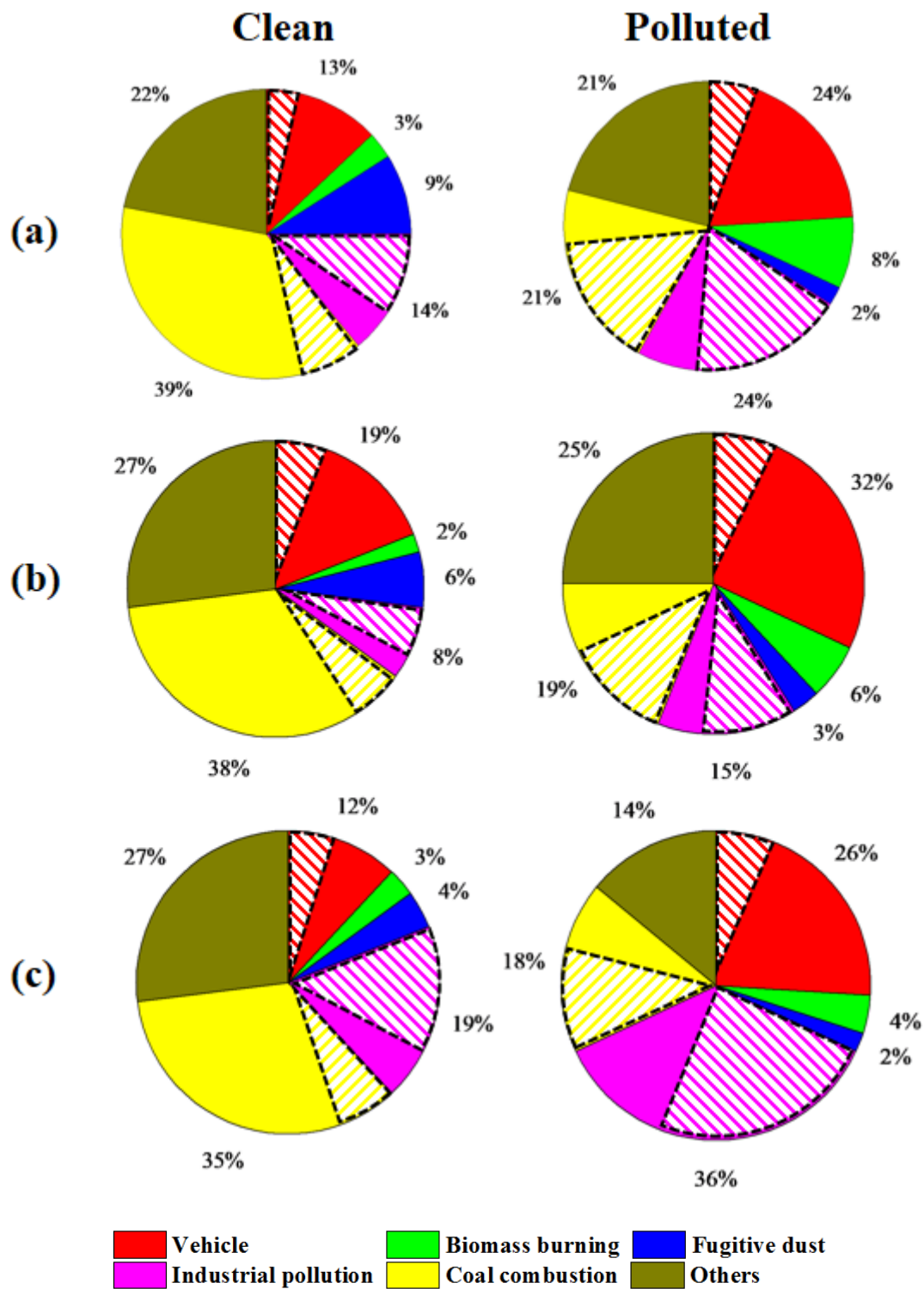1044

1045 **Figure 6**

1046

1048 **Figure 7**

(a)　　　　　　　　(b)　　　　　　　　(c)

(d)　　　　　　　　(e)　　　　　　　　(f)

1049

1050

1051 **Figure 8**